UNIVERSITY OF CALIFORNIA, SAN DIEGO

Imaging large-scale cellular activity in spinal cord of freely behaving mice

A dissertation submitted in partial satisfaction of the requirements for the degree
Doctor of Philosophy

in

Biology

by

Kohei Sekiguchi

Committee in Charge:

Professor Axel Nimmerjahn, Chair
Professor Wendy M. Campana
Professor Samuel L. Pfaff
Professor Mark H. Tuszynsky
Professor Yimin Zou

2017

The Dissertation of Kohei Sekiguchi is approved, and it is acceptable in quality and form for publication on microfilm and electronically:

Chair

University of California, San Diego

2017

DEDICATION

This dissertation is dedicated to my family, friends and mentors near and far, who continuously supported, encouraged and inspired me through my entire Ph.D. process.

TABLE OF CONTENTS

LIST OF FIGURES

ACKNOWLEDGEMENTS

Foremost, I would like to thank my Ph.D. advisor Professor Axel Nimmerjahn, for providing me with the great opportunity to pursue my Ph.D. research. I am very greatful for his experience, passion and mentorship, which made my Ph.D. research unique and intriguiding. I would also like to express my gratitude to my committee members, Professor Wendy M. Campana, Professor Samuel L. Pfaff, Professor Mark H. Tuszynsky, and Professor Yimin Zou for serving as my committee members and providing constructive advice and inspirational ideas on my research.

I wish to thank the past and present Nimmerjahn lab members, for their assistance and friendship. Special thanks to Pavel Shekhtmeyster, who supported me inside and outside of the lab.

My great appreciation goes to all my friends I met in San Diego. Special thanks to Salk soccer team members, who warmly welcomed me as a member and made me smile whenever we get together.

I acknowledge the fellowships, Jesse and Caryl Philips Foudations, Mary K.Chapman and the Nakajima Foundtation. They financially supported me to obtain Ph.D. for years.

Finally, I would like to thank my family members. My parents Takahiro and Masako Sekiguchi, for their generous support to obrain Ph.D. at University of California, San Diego.

Chapter 2 is an adaptation of Sekiguchi K.J., Shekhtmeyster P., Merten K., Arena A., Cook D., Hoffman E., Ngo A., Nimmerjahn A. Imaging large-scale cellular activity in spinal cord of freely behaving mice. Nat. Commun. (2016). The dissertation author was primary author.

VITA

2007-2011	University of Tokyo Bachelor of Science, Molecular Biology
2011-2017	University of California, San Diego The Salk Institute for Biological Studies Doctor of Philosophy, Biology

FELLOWSHIPS

2011-2016	Recipient of the Nakajima Foundation Predoctoral Fellowship
2012-2013	Recipient of Jesse and Caryl Philips Foudations
2013-2016	Recipient of Mary K. Chapman

PUBLICATIONS

Knowland D, Arac A, **Sekiguchi KJ**, Hsu M, Lutz SE, Perrino J, Steinberg GK, Barres BA, Nimmerjahn A, Agalliu D.
Stepwise recruitment of transcellular and paracellular pathways underlies blood-brain barrier breakdown in stroke.
Neuron **82**, 603-17 (2014)

Sekiguchi KJ, Shekhtmeyster P, Merten K, Arena A, Cook D, Hoffman E, Ngo A, Nimmerjahn A.
Imaging large-scale cellular activity in spinal cord of freely behaving mice.
Nat. Commun. **7**, e11450 (2016)

Tufail Y, Cook S, Fourgeaud L. Powers CJ, Merten K, Clark CL, Hoffman E, Ngo A, **Sekiguchi KJ**, O'Shea CC, Lemke G, Nimmerjahn A.
Phosphatidylserine exposure controls viral innate immune responses by microglia.
Neuron **93**, 574-86 (2017)

ABSTRACT OF THE DISSERTATION

Imaging large-scale cellular activity in spinal cord of freely behaving mice

by

Kohei Sekiguchi

Doctor of Philosophy in Biology

University of California, San Diego, 2017

Professor Axel Nimmerjahn, Chair

Sensory information from mechanoreceptors and nociceptors in the skin plays key roles in adaptive and protective motor behaviors. To date, very little is known about how this information is encoded by spinal cord cell types and their activity patterns, particularly under freely behaving conditions. To enable stable measurement of neuronal and glial cell activity in behaving mice, we have developed fluorescence imaging approaches based on two- and miniaturized one-photon microscopy. We show that distinct cutaneous stimuli activate overlapping ensembles of dorsal horn neurons, and that stimulus type and intensity is encoded at the single cell level. In contrast, astrocytes show large-scale coordinated calcium responses to intense but not weak sensory inputs. Sensory-evoked activity is potently suppressed by anesthesia. By revealing the cellular and computational logic of spinal cord networks under behaving conditions our approach holds promise for better understanding of healthy and aberrant spinal cord processes.

Chapter 1
Introduction

Anatomy of the somatosensory system

A longstanding goal in neuroscience research has been to decipher how nervous system activity relates to changes in our environment and how it controls animal behavior. In particular, the somatosensory system is crucial for processing sensory information and guiding adaptive/protective motor behaviors. It consists of three main constituents: a) primary afferent neurons of the peripheral nervous system, b) cellular circuits in the spinal dorsal horn, and c) cellular networks across multiple brain regions (e.g., the parabrachial nucleus (PB) of the dorsolateral brainstem, the midbrain periaqueductal gray (PAG), the reticular formation, hypothalamus, thalamus, and somatosensory cortex) (1–5).

Somatosensory processing in the spinal cord

The cell bodies of primary afferent neurons are located in the dorsal root ganglia (DRG). The axonal branches they extend connect peripheral and central targets (e.g., the skin and spinal cord) (6, 7). Different peripheral targets are innervated by distinct primary afferents, which in turn project to different spinal cord regions (8, 10, 13, 14). Primary afferents innervating the same peripheral target are generally equipped with distinct sets of receptors which allow them to sense, for example, mechanical or thermal stimuli (6–12). These different types of sensory stimuli, transmitted by the distinct subpopulations of primary afferents (C, Aδ, Aβ fibers) (6, 7), are then relayed to defined lamina within the spinal dorsal horn (e.g., myelinated Aδ fibers convey innocuous mechanical inputs and pain signals to lamina I) (15). Activated primary afferents can secrete neurotransmitters, such as glutamate or neuropeptides, which in turn activate specific subsets of dorsal horn neurons.

Various types of neurons in the dorsal horn, including inhibitory and excitatory neurons,

receive primary afferent input (16, 17). Activation of these neurons is a key component of somatosensory information processing (18, 19). In addition, neurons in the dorsal horn receive supraspinal input from the brain (6, 7). These descending projections can modulate sensory information processing by secreting broadly acting neuromodulators, such as norepinephrine or serotonin, or by directly contacting specific subsets of inhibitory neurons. Information processed by dorsal horn neurons is then typically relayed to upstream brain regions (e.g., the brain stem or thalamus) through projection neurons (10, 20, 21). Nevertheless, very little is known about how the activity patterns of neurons within the dorsal horn encode sensory input, despite it being the first processing stage/integration center within the central nervous system (CNS). This is largely due to a lack of techniques that allow high-resolution measurement of cellular activity in the spinal cord under natural/behaving conditions.

The role of astrocytes in somatosensory processing

Dorsal horn neurons are embedded in a dense network of glial cells. In particular, astrocytes are one of the most abundant glial cell types in the CNS. Astrocyte processes physically and chemically interact with neuronal synapses. Neurotransmitter receptors on these processes allow astrocytes to sense neuronal activity. In the brain, neurotransmitters such as glutamate, ATP, or norepinephrine have been shown to evoke different forms of Ca^{2+} excitation in astrocytes (23, 24, 25). The downstream effects of astrocyte calcium excitation are still debated but may include changes in synapse ensheathment, transporter expression, and release of neuro-active substances, such as ATP, D-serine, or cytokines. In the dorsal horn, astrocytes have been shown capable of secreting diffusible messengers in response to repeated C fiber activation, which can lead to long-term potentiation of susceptible synapses at distant sites (i.e., outside the receptive field) (26). This suggests that astrocytes are capable of modulating neural circuit properties and potentially animal behavior in unique ways (22). However, whether and how neuron-astrocyte communication contributes to sensory processing under behaving conditions

remains unclear. This, again, is largely due to a lack of techniques that allow measurement of astrocyte Ca^{2+} excitation in response to sensory or nociceptive input under natural conditions. Furthermore, it is unclear whether the mechanisms governing astrocyte calcium excitation in the brain (27) apply to the spinal cord, which is anatomically and functionally different.

Tools to study somatosensory processing *in vivo*

To determine cell and circuit function, electrophysiological approaches have traditionally been used to record from single electrically excitable cells such as neurons (28, 29). In the brain, these approaches have provided a number of surprising insights into how neurons compute incoming information and how they control behavior, both in awake head-restrained (30–32) or freely moving animals (33–38). In the spinal cord, however, electrophysiological approaches have been less successful. This is, at least in part, due to the difficulty of controlling spinal cord movement due to breathing or animal behavior, and the sensitivity of the spinal cord to tissue disturbances (e.g., microelectrode insertion). Electrophysiological approaches are also inherently ill suited for recording from electrically unexcitable cells such as astrocytes.

Optical imaging approaches in conjunction with fluorescent calcium indicators have recently enabled minimally invasive and comprehensive recording of neuronal and astrocyte activity in behaving animals. For example, while multi-photon imaging has enabled comprehensive sampling from dense networks of neurons and astrocytes in sensory cortex of head-restrained mobile mice (39), miniaturized microscopy has enabled optical recordings from freely moving rodents (40, 41). This has led to the discovery of unanticipated forms of neuronal and astrocyte excitation in multiple brain regions (27, 42, 43). However, whether these techniques and corresponding genetic and molecular tools can be adapted for minimally invasive and stable measurement of cellular activity in the spinal cord of behaving animals has remained unclear. Their successful application promises to yield new insights into how neurons encode sensory information and how they recruit astrocytes under natural conditions.

References

1. Bernard, J.F., Dallel, R., Raboisson, P., Villanueva, L. & Le Bars, D. Organization of the efferent projections from the spinal cervical enlargement to the parabrachial area and periaqueductal gray: a PHA-L study in the rat. *J. Comp. Neurol.* **353**, 480–505 (1995).

2. Burstein, R., Cliffer, K.D. & Giesler, G.J., Jr. Cells of origin of the spinohypothalamic tract in the rat. *J. Comp. Neurol.* **291**,329–344 (1990).

3. Todd, A.J., McGill, M.M. & Shehab, S.A. Neurokinin 1 receptor expression by neurons in laminae I, III and IV of the rat spinal dorsal horn that project to the brainstem. *Eur. J. Neurosci.* **12**, 689–700 (2000).

4. Al-Khater, K.M. & Todd, A.J. Collateral projections of neurons in laminae I, III, and IV of rat spinal cord to thalamus, periaqueductal gray matter, and lateral parabrachial area. *J. Comp. Neurol.* **515**, 629–646 (2009).

5. Spike, R.C., Puskar, Z., Andrew, D. & Todd, A.J. A quantitative and morphological study of projection neurons in lamina I of the rat lumbar spinal cord. *Eur J Neurosci.* 18, 2433–2448 (2003).

6. Kandel, E., Schwartz, J., Jessell, T., Siegelbaum, S. & Hudspeth, A.J. Principles of Neural Science, 5th Edn. McGraw Hill Professional (2012).

7. Purves, D., Augustine, G.J., Fitzpatrick, D., Hall, W.C., LaMantia, A.S. & White, L.E. Neuroscience, 5th Edn. Sinauer Associates, Inc. (2012).

8. Averill, S., McMahon, S.B., Clary, D.O., Reichardt, L.F. & Priestley, J.V. Immunocytochemical localization of trkA receptors in chemically identified subgroups of adult rat sensory neurons. *Eur. J. Neurosci.* **7**, 1484–1494 (1995).

9. McCoy, E.S., Taylor-Blake, B., Street, S.E., Pribisko, A.L., Zheng, J. & Zylka, M.J. Peptidergic CGRPα primary sensory neurons encode heat and itch and tonically suppress sensitivity to cold. *Neuron* **78**, 138–15 (2013).

10. Abraira V.E. & Ginty D.D. The sensory neurons of touch. *Neuron* **79**, 618–639 (2013).

11. Zotterman Y. Touch, pain and tickling: an electro-physiological investigation on cutaneous sensory nerves. *J. Physiol.* **95**, 1–28 (1939).

12. Basbaum, A.I., Bautista, D.M., Scherrer, G. & Julius, D. Cellular and molecular mechanisms of pain. *Cell* **139**, 267–284 (2009).

13. Vrontou, S., Wong, A.M., Rau, K.K., Koerber, H.R., Anderson, D.J. Genetic identification of C fibres that detect massage-like stroking of hairy skin *in vivo*. *Nature* **493**, 669–673 (2013).

14. Li, L., Rutlin, M., Abraira, V.E., Cassidy, C., Kus, L., Gong, S., Jankowski, M.P., Luo, W., Heintz, N., Koerber, H.R., Woodbury, C. J. & Ginty, D. D. The functional organization of cutaneous low-threshold mechanosensory neurons. *Cell* **147**, 1615–1627 (2011).

15. Zheng, J., Lu, Y. & Perl, E.R. Inhibitory neurones of the spinal substantia gelatinosa mediate interaction of signals from primary afferents. *J. Physiol.* **588**, 2065–2075 (2010).

16. Grudt, T.J. & Perl, E.R. Correlations between neuronal morphology and electrophysiological features in the rodent superficial dorsal horn. *J. Physiol.* **540**, 189–207 (2002).

17. Bernard, J.F., Dallel, R., Raboisson, P., Villanueva, L. & Le Bars, D. Organization of the efferent projections from the spinal cervical enlargement to the parabrachial area and periaqueductal gray: a PHA-L study in the rat. *J Comp Neurol.* **353**, 480–505 (1995).

18. Bourane, S., Duan, S., Koch, S.C., Dalet, A., Garcia-Campmany, L., Kim, E., Cheng, L., Ma, Q. & Goulding, M. Gate control of mechanical itch by a subpopulation of spinal cord interneurons. *Science* **350**, 550-554 (2015)..

19. Bourane, S., Grossmann, K.S., Britz, O., Del Barrio, M.G., Stam, F.J., Garcia-Campmany, L., Koch, S. & Goulding, M. Identification of a spinal circuit for light touch and fine motor control. *Cell* **160**, 503-515 (2015).

20. Burstein, R., Cliffer, K.D. & Giesler, G.J. Jr. Cells of origin of the spinohypothalamic tract in the rat. *J Comp Neurol.* **291**, 329–344 (1990).

21. Todd, A.J. Neuronal circuitry for pain processing in the dorsal horn. *Nat Rev Neurosci.* **11**, 823–836 (2010).

22. Shiratori-Hayashi, M., Koga, K., Tozaki-Saitoh, H., Kohro, Y., Toyonaga, H., Yamaguchi, C., Hasegawa, A., Nakahara, T., Hachisuka, J., Akira, S., Okano, H., Furue, M., Inoue, K. & Tsuda, M. STAT3-dependent reactive astrogliosis in the spinal dorsal horn underlies chronic itch. *Nat. Med.* **21**, 927-931 (2015).

23. Fiacco, T.A. & McCarthy, K.D. Astrocyte calcium elevations: Properties, propagation, and effects on brain signaling. *Glia* **54**,676–690 (2006).

24. Paukert, M., Agarwal, A., Cha, J., Doze, V.A., Kang, J.U. & Bergles, D.E. Norepinephrine controls astroglial responsiveness to local circuit activity. *Neuron* **82**, 1263-70 (2014).

25. Wang, X., Lou, N., Xu, Q., Tian, G.F., Peng, W.G., Han, X., Kang, J., Takano, T. & Nedergaard, M. Astrocytic Ca^{2+} signaling evoked by sensory stimulation *in vivo*. *Nat. Neurosci.* **6**, 816–823 (2006).

26. Kronschläger, M.T., Drdla-Schutting, R., Gassner, M., Honsek, S.D., Teuchmann, H.L. & Sandkühler, J. Gliogenic LTP spreads widely in nociceptive pathways. *Science* **354**, 1144-1148 (2016).

27. Srinivasan, R., Huang, B.S., Venugopal, S., Johnston, A.D., Chai, H., Zeng, H., Golshani, P. & Khakh, B.S. Ca^{2+} signaling in astrocytes from $Ip3r2^{(-/-)}$ mice in brain slices and during startle responses *in vivo*. *Nat. Neurosci.* **18**, 708-717 (2015).

28. Kato, G., Kawasaki, Y., Koga, K., Uta, D., Kosugi, M., Yasaka, T., Yoshimura, M., Ji, R.R. & Strassman, A.M. Organization of intralaminar and translaminar neuronal

connectivity in the superficial spinal dorsal horn. *J Neurosci.* **29**, 5088–5099 (2009).

29. Wu, S.X., Wang, W., Li, H., Wang, Y.Y., Feng, Y.P. & Li, Y.Q. The synaptic connectivity that underlies the noxious transmission and modulation within the superficial dorsal horn of the spinal cord. *Prog Neurobiol.* **91**, 38–54 (2010).

30. Harvey, C.D., Collman, F., Dombeck, D.A. & Tank, D.W. Intracellular dynamics of hippocampal place cells during virtual navigation. *Nature* **461**, 941-946 (2009).

31. Houweling, A.R. & Brecht, M. Behavioural report of single neuron stimulation in somatosensory cortex. *Nature* **451**, 65-68 (2008).

32. Niell, C.M. & Stryker, M.P. Modulation of visual responses by behavioral state in mouse visual cortex. *Neuron* **65**, 472-479 (2010).

33. Lee, A.K., Manns, I.D., Sakmann, B. & Brecht, M. Whole-cell recordings in freely moving rats. *Neuron* **51**, 399-407 (2006).

34. Burgalossi, A., Herfst, L. von Heimendahl, M., Forste, H., Haskic, K., Schmidt, M. & Brecht, M. Microcircuits of functionally identified neurons in the rat medial entorhinal cortex. *Neuron* **70**, 773-786 (2011).

35. Epsztein, J., Lee, A.K., Chorev, E. & Brecht, M. Impact of spikelets on hippocampal CA1 pyramidal cell activity during spatial exploration. *Science* **327**, 474-477 (2010).

36. Foster DJ, Wilson MA: Reverse replay of behavioural sequences in hippocampal place cells during the awake state. *Nature* **440**, 680-683 (2006).

37. Harris, K.D., Henze, D.A., Hirase, H., Leinekugel, X., Dragoi, G., Czurko, A. & Buzsaki, G. Spike train dynamics predicts theta-related phase precession in hippocampal pyramidal cells. *Nature* **417**,738-741 (2002).

38. Szuts, T.A., Fadeyev, V., Kachiguine, S., Sher, A., Grivich, M.V., Agrochao, M., Hottowy, P., Dabrowski, W., Lubenov, E.V., Siapas, A.G., Uchida, N., Litke, A.M. & Meister, M. A wireless multi-channel neural amplifier for freely moving animals. *Nat. Neurosci.* **14**, 263-269 (2011).

39. Dombeck, D.A., Khabbaz, A.N., Collman, F., Adelman, T.L. & Tank, D.W. Imaging large-scale neural activity with cellular resolution in awake, mobile mice. *Neuron* **56**, 43-57 (2007).

40. Ghosh, K.K., Burns, L.D., Cocker, E.D., Nimmerjahn, A., Ziv, Y., Gamal, A.E. & Schnitzer, M.J. Miniaturized integration of a fluorescence microscope. *Nat. Methods* **8**, 871-878 (2011).

41. Sawinski, J., Wallace, D.J., Greenberg, D.S., Grossmann, S., Denk, W. & Kerr, J.N.D. Visually evoked activity in cortical cells imaged in freely moving animals. Proc Natl Acad Sci. U S A **106**, 19557-19562 (2009).

42. Kato, H.K., Gillet, S.N., Peters, A.J., Isaacson, J.S. & Komiyama, T. Parvalbumin-expressing interneurons linearly control olfactory bulb output. *Neuron* **80**, 1218-1231 (2013).

43. Ziv, Y., Burns, L.D., Cocker, E.D., Hamel, E.O., Ghosh, K.K., Kitch, L.J., El Gamal, A. & Schnitzer, M.J. Long-term dynamics of CA1 hippocampal place codes. *Nat. Neurosci.* **16**, 264-266 (2013).

Chapter 2
Imaging large-scale cellular activity in spinal cord of freely behaving mice

Abstract

Sensory information from mechanoreceptors and nociceptors in the skin plays key roles in adaptive and protective motor behaviors. To date, very little is known about how this information is encoded by spinal cord cell types and their activity patterns, particularly under freely behaving conditions. To enable stable measurement of neuronal and glial cell activity in behaving mice, we have developed fluorescence imaging approaches based on two- and miniaturized one-photon microscopy. We show that distinct cutaneous stimuli activate overlapping ensembles of dorsal horn neurons, and that stimulus type and intensity is encoded at the single cell level. In contrast, astrocytes show large-scale coordinated calcium responses to intense but not weak sensory inputs. Sensory-evoked activity is potently suppressed by anesthesia. By revealing the cellular and computational logic of spinal cord networks under behaving conditions our approach holds promise for better understanding of healthy and aberrant spinal cord processes.

Introduction

Deciphering how cellular activity in the central nervous system (CNS) encodes sensory information and animal behavior remains one of the greatest challenges in neuroscience research today. Traditionally, electrophysiological approaches have been used to sparsely sample from electrically excitable cells. Optical imaging in combination with new labeling approaches now allows minimally invasive and comprehensive sampling from dense networks of both electrically and chemically excitable cells, such as neurons and glial cells (1). Imaging in head-restrained mobile mice and with miniaturized head-borne microscopes, for example, has led to the discovery of unanticipated forms of behaviorally related neuronal and astrocyte excitation in cortical and

deep brain microcircuits (2–5). Application of these imaging modalities to the spinal cord, the primary neurological link between the brain and other parts of the body, promises to yield new insight into how genetically defined cell types and their activity patterns contribute to spinal cord physiology and animal behavior. In particular, given its ordered cellular arrangement, the spinal cord presents unique opportunities for studying neuron-glia communication and its role in CNS function (6, 7).

Spinal dorsal horn circuits are involved in sensory information processing, including pain perception (8, 9). How neuronal components that make up these circuits encode information coming from skin or deeper tissues is unclear. Likewise, dorsal horn astrocytes structurally and functionally interact with spinal neurons and contribute to pain sensation (10–12). How astrocyte activity relates to spinal neuron spiking, and to what extent these cells encode sensory information in behaving mice is unknown.

To enable stable measurement of neuronal and astrocyte activity in the spinal cord of behaving mice, we further developed fluorescence imaging approaches based on two- and miniaturized one-photon microscopy and, by comparing the two modalities in the same animal, we provide practical guidelines for their future use in the CNS. We demonstrate that distinct cutaneous inputs in awake mice activate partially overlapping subsets of neurons, and that type and intensity of sensory information is encoded at the single neuron level. In contrast, sensory stimulus parameters appeared only weakly reflected in individual calcium transients from dorsal horn astrocytes. Astrocyte population activity, including large-scale coordinated calcium transients in response to high- but not low-intensity sensory stimulation, correlated with certain aspects of sensory input. General anesthesia potently suppressed calcium activity in both dorsal horn neurons and astrocytes.

Results

Fluorescence imaging in spinal cord of freely behaving mice

As a first step toward optical recording of cellular dynamics in the spinal cord of behaving mice, we created custom miniaturized one-photon microscopes for high-speed fluorescence imaging with subcellular resolution, similar to our previous work (3, 5) (Figure 2.1a). We established a spinal cord window preparation for in vivo imaging of spinal dorsal horn (13), and for stable attachment of our 2.5-gram (g) miniaturized microscope to the animal's back (Figure 2.1a-b). Before and one day after surgical preparation, we quantified the animal's locomotor performance on a motorized linear treadmill. Adult wild type mice implanted with a lumbar spinal cord window and an attached miniaturized microscope showed no overt signs of altered locomotor behavior, even without habituation. Maximum running speed and hind limb stride length values were comparable to the same mice before surgical preparation (Figure 2.1c) (one-way repeated measures ANOVA; $p \geq 0.05$; N = 5 mice per group).

Next, to quantify lateral and axial motion artifacts during imaging we implanted spinal cord windows in transgenic Thy1-eYFP-H mice with sparsely labeled axons (Figure 2.1d) (14). In awake resting mice, image displacements due to breathing or minor body movements occurred primarily in the rostro-caudal direction (mean ± SEM, 8.5 ± 8.0 μm; 75% percentile within 11.2 μm; N = 4 mice), while displacements in the medio-lateral (1.5 ± 0.3 μm; 75% percentile within 2.1 μm ; N = 4 mice) or dorso-ventral direction (≤3 μm; N = 4 mice) were small. Motion artifacts increased in amplitude during steady walking or running but remained largely confined to the rostro-caudal direction (22.3 ± 16.8 μm; 75% percentile within 29.1 μm; N = 4 mice) with only small increases in medio-lateral (3.2 ± 1.6 μm; 75% percentile within 3.9 μm; N = 4 mice) or dorso-ventral image displacement (≤5 μm, respectively; N = 4 mice) (Figure 2.2a-b), allowing continuous video-rate tracking of cells within central regions of the 350 μm x 700 μm effective field of view. Image displacements were largely uniform across the field of view, allowing automated or manual subpixel registration (15). During certain movements, such as grooming or left/right side bending of the spinal cord (e.g., when the animal made a sharp turn), image displacements across the field of view were non-uniform, typically increasing with distance from

the central vein. We restricted our motion artifact analysis to dorsal horn regions.

To determine attainable imaging depth with our miniaturized one-photon microscopes we made use of transgenic mice expressing tdTomato in genetically defined dorsal horn neurons with known laminar distribution (16, 17) (Figure 2.3a). Imaging the same dorsal horn region with two-photon and miniaturized one-photon microscopy in anesthetized mice with labeled somatostatin lineage neurons (SOM-tdTomato mice) revealed that cells located as deep as outer lamina II are readily accessible with both imaging modalities (Figure 2.3b-c). This enables optical monitoring of cellular circuits involved in sensory or pain processing (8, 9). The extended depth of field of one- as compared to two-photon microscopy allowed concomitant monitoring of cells located at different depth (Figure 2.3b-c) and, for a given image sensor frame acquisition rate, across a larger field of view than point scanning-based two-photon microscopy.

Fluorescence imaging in spinal cord of awake mobile mice

When imaging small-scale structures such as single axons, two-photon microscopy provided superior contrast and spatial resolution (Figure 2.4), and optical access to dorsal horn regions below outer lamina II. Given these particular advantages, we sought to implement approaches for two-photon imaging in spinal cord of awake mobile mice (Figure 2.5a-b). Restraining mice at the level of the implanted spinal cord chamber, analogous to head-restrained brain imaging (2, 4), resulted in reduced maximum and average running speed of mice on a spherical treadmill (Figure 2.5c) (one-way repeated measures ANOVA; $p < 0.05$; $N = 5$ mice per group). Likewise, duration of running was reduced compared to head-restrained mice (Figure 2.5c) (one-way repeated measures ANOVA; $p < 0.05$; $N = 6$ mice per group). However, when we restrained mice both at the level of the spinal cord and head, using implanted chambers on either site, mice showed locomotor performance comparable to head-restrained mice (Figure 2.5c) (one-way repeated measures ANOVA; $p \geq 0.05$; $N = 6$ mice per group). The additional head restraint prevented mice from left/right bending of their upper body and further reduced motion artifacts.

To quantify lateral and axial motion artifacts during two-photon imaging in awake mobile mice, we performed video-rate optical recordings in transgenic Thy1-eYFP-H mice (Figure 2.5d). As in the case of freely moving mice, image displacements occurred primarily in the rostro-caudal direction during awake resting and running periods (7.5 ± 7.1 μm, 75% percentile within 10.5 μm and 21.9 ± 17.3 μm, 75% percentile within 29.9 μm, respectively; N = 3 mice) (Figure 2.6a-b). Medio-lateral and dorso-ventral image displacements were generally small in both awake resting (1.5 ± 0.2 μm, 75% percentile within 2.0 μm and ≤3 μm, respectively; N = 3 mice) and running mice (3.0 ± 0.9 μm, 75% percentile within 4.0 μm and ≤5 μm, respectively; N = 3 mice) (Figure 2.6a-b), allowing continuous tracking of cells at 30.9 fps for most behaviors within central regions of the 270 μm x 360 μm effective field of view without adaptive focus control (18).

Sensory information encoding by dorsal horn neurons

Having established and compared two- and miniaturized one-photon imaging in spinal cord of behaving mice, we proceeded with functional measurements based on changes in intracellular calcium concentration. To monitor calcium activity in dorsal horn neurons we injected AAV9-CaMKII-GCaMP6f at the lumbar (L4-L5 vertebra) level 14 days prior to spinal cord window implantation (Figure 2.7a-d). Calcium imaging using miniaturized one-photon microscopy was performed immediately after spinal cord window implantation. In anesthetized mice, a subset of fluorescently labeled neurons across the field of view reliably responded to focal pinch to the base of the animal's tail with a latency of ~0.5 s (Figure 2.8a-d; Methods). Tail pinch with calibrated forceps (see Methods) was chosen because it can be readily and reproducibly applied in awake mice (19). Focal pinch to the animal's hind paws elicited little or no discernible calcium transients.

To gain deeper insight into how dorsal horn neurons encode pinch, we systematically varied pinch duration while keeping other stimulus parameters such as pressure amplitude or position constant (Figure 2.8e). Using a cell-sorting algorithm based on principal and independent

component analysis (PCA/ICA) (20) supplemented by manual region of interest (ROI) analysis (see Methods), population calcium imaging data from 37 cells in 4 mice revealed a linear relationship between pinch and calcium transient duration (R^2=0.75 ± 0.04; n = 37 cells in N = 4 mice) (Figure 2.8f). When we varied pinch pressure, while keeping pinch duration and position constant, individual neurons' calcium transient amplitude showed a steady but non-linear increase (Figure 2.9a-b). Two-photon measurement of the same cells confirmed these findings (Figure 2.10). We also found that the number of activated dorsal horn neurons increased with pinch pressure (Figure 2.9c).

Next, we asked how cellular response properties differ between anesthetized and awake mice. Repeating above pinch experiments in the same mice after they had recovered from isoflurane anesthesia for at least 1.5 hours we found that the calcium transient-to-stimulus duration relationship still showed a largely linear relationship (R^2=0.67 ± 0.05; n = 68 cells in N = 4 mice) (Figure 2.8e-f). However, a larger number of neurons responded to a given pinch pressure (Figure 2.9a-c). Closer examination of pinch-evoked responses of individual neurons under anesthetized and awake conditions revealed that general anesthesia decreased responsiveness of dorsal horn neurons (Figure 2.9b-c).

To test whether dorsal horn neural activity may be modulated by behavioral state, we tracked animals' behavior in their home cage using video recordings. In awake resting mice, spontaneous firing of labeled dorsal horn neurons was low but increased compared to the same mice under anesthesia (0.52 ± 0.15 Hz and 0.08 ± 0.04 Hz, respectively; n = 28 cells in N = 4 mice; paired t-test with Welch's correction; $p < 0.05$) (Figure 2.9d). Locomotor activity further increased neuronal firing rate (1.10 ± 0.11 Hz; n = 28 cells in N = 4 mice; paired t-test with Welch's correction; $p < 0.05$) (Figure 2.9d), but did not evoke spatiotemporal patterns of neural activity seen in response to pinch. Pinch-evoked calcium transients reliably occurred at pinch onset and their duration was tightly correlated with stimulus duration (Figure 2.8c-f).

Having characterized the response properties of dorsal horn neurons to pinch, we next

asked how the same neurons (n = 211 cells in N = 3 mice) respond to different types of cutaneous stimuli. When we applied an air puff to the base of the animal's tail under anesthetized or awake conditions, a distinct subset of labeled dorsal horn neurons responded reliably (Figure 2.11a-b). Some neurons preferentially responded to air puff (n = 21 cells in N = 3 mice), while others responded to pinch only (n = 61 cells in N = 3 mice) (Figure 2.11c; Figure 2.13). Around 20% of pinch-responsive neurons responded reliably to air puff (n = 21 cells in N = 3 mice; 25 air puffs) (Figure 4d). When mice groomed their hindquarters, near the base of their tail, a large subset of pinch-responsive neurons (69.7%; n = 46 cells in N = 2 mice; 14 grooming events) responded with calcium transients (Figure 2.12 a-d). No such response was seen when mice engaged in forequarter grooming. In contrast to "pinch" and "air puff"-responsive cells, neurons that were activated by self-initiated hindquarter grooming appeared more evenly distributed throughout dorsal horn at the L4-L5 vertebra level (Figure 2.11b, 2.12b). These results demonstrate that distinct cutaneous stimuli to the same bodily region can recruit different, partially overlapping ensembles of dorsal horn neurons.

Sensory information encoding by dorsal horn astrocytes

Dorsal horn neurons are embedded in a dense network of spinal cord astrocytes. Astrocytes structurally and functionally interact with neurons in spinal cord and brain. Astrocytes show neuronal activity-dependent forms of calcium excitation. In cortical regions of behaving mice, different spatiotemporal forms of astrocyte calcium activity have been identified (21). However, it is unknown what forms of astrocyte calcium activity exist in the spinal cord, and how these transients relate to calcium spiking in spinal neurons of behaving mice. To begin to address this question we transduced spinal cord astrocytes at the L4-L5 vertebra level with AAV5-GfaABC1D-GCaMP6f 21 days prior to spinal cord window preparation (Figure 2.7e-f). Imaging was performed on the day of window implantation. While miniaturized one-photon microscopy allowed large dorsal horn areas to be monitored in freely moving mice, its limited spatial resolution

and the dense labeling of astrocytes and their fine processes hampered reliable detection of astrocyte microdomain activations. To monitor calcium activity in astrocyte fine processes and somata of lamina I and II, we performed two-photon imaging in awake mice on a spherical treadmill, restrained at the spinal cord and head level and after they had recovered from isoflurane anesthesia for at least 1.5 hours.

In awake resting mice, calcium transient frequency in processes of dorsal horn astrocytes was low but elevated compared to the same mice under anesthesia (2.91 ± 0.06 transients per min and 0.53 ± 0.12 transients per min, respectively; n = 84 ROIs in N = 4 mice; paired t-test with Welch's correction; $p < 0.05$) (Figure 2.14 a-c). Process activity was further increased in running animals (4.83 ± 0.15 transients per min; n = 84 ROIs in N = 4 mice) (Figure 5a-c). Unlike in the cortex (4, 22, 23), running alone did not evoke large-scale coordinated calcium events (Figure 2.14a). Amplitude and duration of calcium transients in astrocyte processes was comparable between anesthetized, awake resting, and running mice (Figure 2.14c) (one-way ANOVA with Tukey-Kramer's multiple comparisons test; $p \geq 0.05$; n = 84 ROIs in N = 4 mice per group).

Low- (P = 30-70 g) or medium-amplitude (P = 130-220 g) pinch to the base of the animal's tail led to a modest increase in the frequency of astrocyte process activations, but no significant change in calcium transient amplitude or duration in anesthetized (0.85 ± 0.19 transients per min, 286 ± 72 % ΔF/F, 1.13 ± 0.40 s or 1.28 ± 0.20 transients per min, 235 ± 93 % ΔF/F, 0.92 ± 0.25 s, respectively) or awake mice (7.75 ± 0.52 transients per min, 295 ± 14 % ΔF/F, 0.98 ± 0.11 s or 8.29 ± 0.71 transients per min, 261 ± 17 % ΔF/F, 0.97 ± 0.10 s, respectively; unpaired t-test with Welch's correction; $p < 0.05$; one-way ANOVA with Tukey-Kramer's multiple comparisons test; $p \geq 0.05$; n = 84 ROIs in N = 4 mice) (Figure 2.14d). Unlike calcium spiking in dorsal horn neurons, astrocyte calcium transients that occurred during pinch had variable delay with respect to stimulus onset, and their duration did not significantly increase with pinch duration in anesthetized or awake mice (R^2=0.05 ± 0.02 or R^2=0.03 ± 0.01, respectively; n = 37 ROIs in N = 4 mice) (Figure 2.14e-f). However, when we increased pinch pressure we found that high-amplitude (P = 400-800 g)

stimuli evoked, with high probability (63.9 ± 5.9%; n = 97 stimuli in N = 4 mice), large-scale coordinated calcium events in astrocyte processes and somata across the field of view with an onset latency of ~3.75 ± 0.22 s (n = 62 events in N = 4 mice) (Figure 2.15a-f; Methods). The average amplitude of individual calcium transients within large-scale events was larger than that of unsynchronized transients in astrocyte processes (469 ± 16 % ΔF/F and 308 ± 6 % ΔF/F, respectively; unpaired t-test with Welch's correction; n = 71 ROIs in N = 4 mice; $p < 0.05$) (Figure 2.15d). The duration of the coordinated population event (2.77 ± 0.15 s; n = 62 events in N = 4 mice) was longer than the duration of individual transients contributing to the large-scale event (1.19 ± 0.03 s; unpaired t-test; n = 71 ROIs in N = 4 mice; $p < 0.05$) (Figure 2.15e).

High-amplitude pinch stimuli tended to evoke locomotor activity (94.8 ± 2.6 % of P ≥ 400 g stimuli; maximum running speed, 80.3 ± 3.6 mm per s; n = 97 stimuli in N = 4 mice). However, the latency of large-scale calcium transients in astrocytes was more tightly correlated with pinch onset than with locomotor activity (Figure 2.15f-g). No correlation was found with either pinch offset or running offset (Figure 2.15f-g). Locomotor activity alone did not evoke large-scale calcium events (Figure 2.14a, 2.15a, 2.15c). Low- or medium-amplitude pinch stimuli also tended to evoke locomotor activity (74.9 ± 8.8 % or 83.2 ± 7.7 % of P = 30-70 g or P = 130-220 g stimuli, respectively; n = 36 or 44 stimuli, respectively, in N = 4 mice) with similar characteristics (maximum running speed, 71.4 ± 5.2 mm per s or 77.0 ± 5.8 mm per s, respectively; Kruskal-Wallis test; n = 36 or 44 stimuli, respectively, in N = 4 mice; $p \geq 0.05$), yet large-scale events occurred significantly less often under these conditions (8.6 ± 3.8 % or 21.6 ± 10.5 % probability, respectively; n = 36 or 44 stimuli, respectively, in N = 4 mice). No large-scale calcium transients were seen under general anesthesia (Figure 2.15c). Large-scale activity occurred bi-laterally and over at least 1 mm in rostro-caudal direction, as revealed by two- and miniaturized one-photon microscopy. Air puff stimulation near the base of the animal's tail was also capable of evoking large-scale astrocyte calcium transients (40% probability; n = 10 stimuli in N = 3 mice). Together, astrocytes in dorsal horn of behaving mice showed spatiotemporal activity patterns and threshold

responses remarkably different from those of dorsal horn neurons.

Discussion

We demonstrate stable imaging of sensory-evoked neuronal activity in spinal cord of freely behaving mice using miniaturized one-photon microscopy. By comparing one- and two-photon recordings of the same cells in the same animal, we provide practical guidelines for future use of the two imaging modalities in behaving mice. We demonstrate that distinct cutaneous stimuli recruit different, overlapping ensembles of dorsal horn neurons. Evoked single cell and population activity in dorsal horn astrocytes showed remarkable differences to dorsal horn neurons, including large-scale coordinated calcium events in response to high- but not low-intensity peripheral stimuli. Unlike gray matter astrocytes of the brain (4, 22, 23), dorsal horn astrocytes did not show large-scale coordinated calcium events triggered by locomotor activity alone. Spinal neuron and astrocyte calcium activity was potently suppressed by general anesthesia.

Miniaturized one-photon microscopy enables stable high-speed optical recording of cellular activity from superficial and deep brain regions in freely moving mice (3, 5, 24–26). We demonstrate that this approach also enables stable cellular activity measurements from spinal cord of freely behaving mice, despite the more pronounced movement of the spine within the vertebral column compared to the brain within the skull (Figure 2.2f and 2.4f) (2, 4). Lateral and axial motion artifacts during optical recordings were comparable between focally restrained and freely moving mice (Figure 2.2f and 2.4f). For animal behaviors associated with large axial movements, including natural behaviors non-executable in restrained mice, volume imaging with vertebra-affixed miniaturized one-photon microscopes offered greater recording stability compared to optical section acquisition with multi-photon microscopy. Camera-based one-photon imaging also allowed monitoring of larger spinal cord areas, or at higher frame rate, compared to point scanning-based two-photon microscopy. The curvature of the spinal cord constrained the number of cells that could be monitored laterally.

Previous studies in anesthetized rodents, using two-photon imaging of non-selective synthetic or genetically encoded calcium indicators, showed that electrical or mechanical peripheral stimulation can evoke calcium spiking in subsets of dorsal horn neurons, with the number of activated neurons depending on stimulus location and intensity (18, 27–29). Additionally, using in utero electroporation of CAG promoter-driven YC-Nano50, Nishida et al. found that pinch, brush, or heat activates partially overlapping subsets of dorsal horn neurons in anesthetized mice (29).

We demonstrate that stimulus-evoked calcium spiking in dorsal horn neurons is potently suppressed by general anesthesia (Figure 2.9a-d) and that in awake mice calcium spiking is modulated by behavioral state (Figure 2.9d), akin to cortical findings (2, 20, 30). By systematically varying pinch parameters, we show that stimulus properties are encoded at the single neuron level (Figure 2.8 and 2.9). Additionally, we found that different types of peripheral stimuli, including tail pinch, air puff, and hindquarter grooming, activated overlapping ensembles of dorsal horn neurons (Figure 2.11b-d, 2.12b-d). While pinch involves activation of mechanoreceptors, air puff and grooming may involve activation of multiple sensory modalities. Future studies in behaving mice are needed to determine how activation of individual sensory or descending pathways contributes to described calcium responses in AAV9-CaMKII-GCaMP6f-transduced cells. Future combined imaging and electrophysiology experiments are needed to address how calcium transients in transduced neurons relate to electrical dorsal horn activity.

Previous studies in anesthetized mice, using two-photon imaging and multi-cell bolus loading of non-selective cell permeant calcium indicator (28, 31), showed that presumed lumbar spinal cord astrocytes can exhibit slow spontaneous calcium oscillations of several seconds duration (28). Calcium transients in response to hind paw stimulation, presumably measured in somatic regions, were also reported (31).

We demonstrate in awake mice that, in the absence of sensory stimulation, astrocyte process activity is infrequent and unsynchronized (Figure 2.14a, c). Calcium transient frequency

depended on behavioral state (Figure 2.14c) and was elevated in response to sensory stimulation (Figure 2.14d). Sensory information was represented differently in dorsal horn astrocytes compared to neurons, based on transients measured in astrocyte processes and neuronal somata. For low- and medium-amplitude stimuli, we found little correlation between the duration of individual calcium transients in astrocyte processes and pinch duration (Figure 2.14e-f), or between calcium transient amplitude in astrocyte processes and pinch pressure (Figure 2.14d). However, large-scale events were evoked primarily by high-amplitude stimuli. General anesthesia markedly suppressed astrocyte calcium transient frequency and eliminated large-scale events (Figure 2.14c-d, 2.15c).

Similar to cortical astrocytes (32), calcium transient frequency in dorsal horn astrocytes was higher in processes compared to somatic regions. Dorsal horn astrocytes showed different forms of calcium excitation (Figure 2.14a, 2.15a-b), including large-scale events. However, unlike large-scale calcium transients described for cortex (4, 22, 23), locomotion alone did not evoke large-scale coordinated calcium excitation in dorsal horn astrocytes (Figure 2.14a, 2.15a, 2.15c), suggesting regional differences in neuron-astrocyte communication or receptor expression. Large-scale events in dorsal horn astrocytes were seen in response to intense sensory stimulation. However, their duration and the duration of their constituent calcium transients was remarkably short compared to cortical events (Figure 2.15a-b, e) (4, 22, 23), indicating differences in astrocyte coupling or intracellular calcium handling. In fact, quantitative PCR data showed different molecular expression of astrocytes in spinal cord compared to one in cortex (12). For example, astrocytes in spinal cord express both inositol triphosphate type 1 and type 2 receptor while astrocytes in cortex express only type 2 receptor, which is one of the key molecules for intracellular calcium handling (33). The long latency of large-scale events (Figure 2.15f) points to a supraspinal trigger that may be linked to stimulus intensity-dependent recruitment of nociceptive fibers and norepinephrine fibers (34, 35).

Future studies are needed to determine how activity patterns in different neuronal

compartments or types of genetically defined sensory neurons (17, 36, 37) relate to calcium excitation in subsets of spinal cord astrocytes and their compartments (12, 38) and how in turn astrocyte calcium activity may influence sensory or pain processing in the spinal cord and brain. Newly developed red-shifted calcium indicator (39) has enabled to record how astrocyte cellular activity correlates neuronal activity of genetically defined population, such as nociceptive fibers and corticospinal inputs. Additionally, the development of indicators for other transmitters, including GABA, opioid and norepinephrine, will soon enable to optically detect a variety of chemical interactions between neurons and glia. These new tools may contribute to the understanding of communication between astrocytes and sensory neurons.

One-photon imaging provides access to superficial spinal cord regions involved in sensory processing. Given that repeated calcium imaging is feasible (Figure 2.16) this together with existing mouse models of disease (40) may allow the study of how cellular activity patterns contribute to disease, and how treatments can control aberrant activity. As an important application of optical imaging in mouse with treatments, several recent studies showed transplanted neural stem cells foster regeneration in spinal cord (41, 42). Optical recording of cellular activity from glia and neurons in the transplanted animals over chronic time scales in combination with behavioral tests may lead discoveries of novel approaches for patients suffering from spina cord injury and disorder.

Optical recordings from deeper regions may be possible using longer wavelength indicators or implantation of micro-optics (3, 43, 44). Optical access to regions beyond those accessible with one-photon microscopy without physical tissue penetration is already possible with multi-photon microscopy (28). However, even latest multi-photon approaches (43, 45), may not be able to reach ventral motor regions, or with high enough signal-to-noise ratio to monitor fast neuronal dynamics because spinal gray matter is largely encased by highly and broadband reflective white matter (46).

Multi-photon imaging generally requires animal restraint, which can limit or alter animal

behavior (1). At the same time, focally restraining animals both at the level of the spinal cord and head, or combining miniaturized microscope-enabled spinal cord with head-restrained recordings presents unique opportunities for concomitant imaging of anatomically connected spinal cord and brain regions (Fig 2.17). This might enable study of how spinal circuit processing shapes sensory perception, or how the brain exerts supraspinal control at the cellular level. Activation of any peripheral region or primary sensory afferent in freely behaving mice can in principle be achieved using opto- or chemogenetic approaches (47–49).

In summary, by producing a dynamic picture of the functioning spinal cord our imaging approaches and their future extensions promise to further our understanding of the computations underlying normal spinal cord processes, and the pathologic changes provoked by spinal cord disorders.

Methods

Animal subjects

All procedures were performed in accordance with the guidelines of the National Institutes of Health (NIH) and were approved by the institutional animal care and use committee (IACUC) at the Salk Institute. Mouse strains used in this study included wild type C57BL6/J (Jackson Laboratories) and transgenic mice (Thy1-eYFP-H, stock #003782, Jackson Laboratories; SOM-Cre x CAG(ROSA-26)-flex-tdTomato, Goulding laboratory, Salk Institute). Mice were typically group-housed at ~22 °C and provided with bedding and nesting material. Both male and (typically) female mice were used with a typical age of 7-10 weeks at the time of imaging (5-7 weeks at the time of stereotactic injection, if performed).

Stereotactic injections

Thin wall glass pipettes were pulled on a Sutter Flaming/Brown micropipette puller (model P-97). Pipette tips were carefully cut at an acute angle under 10x magnification using sterile techniques. Tip diameters were typically ~15-20 μm. Pipettes that did not result with sharp bevels or had larger tip diameters were discarded. Millimeter tick marks were made on each pulled needle to allow measurement of virus volume injected into the spinal cord.

Mice were anesthetized with isoflurane (4% for induction; ~1.5% during surgery) and positioned in a computer-assisted stereotactic system with digital coordinate readout and atlas targeting (Leica Angle Two). Body temperature was maintained at 36-37 °C with a DC temperature controller, and ophthalmic ointment was used to prevent eyes from drying. A small amount of depilator cream (Nair) was used to thoroughly remove hair over dorsal areas of the spinal cord at and around the L4-L5 vertebra level. Skin was cleaned and sterilized with 70% ethanol and betadine. Using surgical scissors a small (~10 mm) incision was made along the midline. Fascia connecting the skin to the underlying muscle were removed with forceps. Skin was held back by retractors, creating an approximately 1” x 1.5” exposed area. Using blunt

dissection, lateral edges of the spinal column were isolated from connective tissue and muscle. Tissue from the vertebra of interest (L4-L5) and one vertebra rostral and caudal to the site of spinal cord exposure was removed with forceps. The spine was then stabilized using Cunningham vertebral clamps and any remaining connective tissue on top of the exposed vertebrae removed with a fine spatula. Using a small sterile needle a ~0.3 mm opening was made in the tissue overlying the designated injection site between the L4 and L5 vertebra. Then, a drop of virus was carefully pipetted onto parafilm (~1-2 μl) for filling the pulled injection needle with the desired volume. Once loaded with sufficient volume, the injection needle was slowly lowered into the spinal cord until the target depth was reached (typically 150-200 μm below the dura). Manual pressure was applied using a 30 mL syringe connected by shrink tubing and 0.6-1.0 μl of virus was slowly injected over a period of ~5-10 minutes. Viruses included AAV9-CaMKII-GCaMP6f (Penn Vector Core; titer, $1.14x10^{13}$ GC per ml; dilution, 1:5; volume, 0.6 μl) and AAV5-GfaABC1D-GCaMP6f (Penn Vector Core; titer, $3.31x10^{13}$ GC per ml; no dilution; volume, 1.0 μl). Once desired volume of virus was injected, the syringe's pressure valve was locked and position maintained for ~10 minutes to allow virus to spread and to avoid backflow upon needle retraction. Following the injection, vertebral clamps were removed and paraspinous muscle approximated over the entry site of the spinal cord. Mice were sutured along the skin incision, given subcutaneous Buprenex SR (0.5 mg per kg) and allowed to recover before placement in their home cage.

Live animal surgery

Spinal imaging chamber and head plate implantation was performed as previously described (13, 50). Animals that received both implants underwent respective surgeries on the same day. Laminectomies (typically 2.0 mm x 4.0 mm wide in medio-lateral and rostra-caudal direction, respectively) were performed at the L4-L5 vertebra level, corresponding to sacral spinal cord. The dura mater overlying the spinal cord was typically kept intact, but removed for repeated

imaging (Figure 2.16). To minimize tissue displacement, it was critical to place the imaging chamber as close to the exposed spinal cord as possible. To achieve this, we modified a previously published design (13). Our chamber included a central opening of 11.2 mm x 5.1 mm with chamfered edges, which improved mechanical stability and reduced mechanical pressure on the spine. Optical windows were sealed with a custom-cut #0 coverslip. Spinal windows were performed either immediately prior to imaging (for Thy1-eYFP-H and SOM-tdTomato mice), or 2-3 weeks after virus injection (14 days for AAV9-CaMKII-GCaMP6f or 21 days for AAV5-GfaABC1D-GCaMP6f). Buprenex SR (0.5 mg per kg) was given to minimize postoperative pain and hypersensitivity (51).

***In vivo* imaging**

For imaging in freely behaving mice, we used miniaturized one-photon microscopes custom-made at the Salk Institute. Compared to our previously published versions (3,5), these microscopes provided a larger field of view (FOV; 720 μm x 960 μm), improved lateral resolution (≤4-6 μm in central regions of the FOV; using an Edmund Optics NT45-549 drum lens, GRINTECH GT-IFRL-200-confD-50 GRIN lens, and Edmund Optics NT45-207 achromatic lens; Figure 2.4), higher sensitivity (6.7 V per lux-sec) and frame rate (45 fps at full resolution; using an Aptina MT9M024 complementary metal-oxide semiconductor (CMOS) image sensor, custom-made headboard, and Aptina AGB1N0CS interface PCB). For imaging of GCaMP6f- or eYFP-expressing cells, the microscope was equipped with a miniature blue light-emitting diode (LXML-PB01-0023, Philips Luxeon Rebel), single-band T495lpxr beamsplitter, ET480/40x excitation filter, and ET535/50m emission filter (Chroma). For imaging of tdTomato-expressing cells, we used a miniature yellow LED (LXML-PX02-0000; Philips Luxeon Rebel), dual-band 59004bs beamsplitter, 59004x excitation filter, and 59004m emission filter (Chroma). A custom-made LED driver was used to correct for LED intensity drift. Typical average power used for imaging was 100-125 μW per mm^2 or 150-175 μW per mm^2 for eYFP / tdTomato- or GCaMP6f-expressing

cells, respectively. Typical image resolution was 1280 x 960 pixels. In a typical imaging session, 80-100 recordings were taken, each lasting ~1-2 min. No signs of phototoxicity, such as a gradual increase in baseline fluorescence, lasting changes in spike rate, or blebbing of labeled cells were apparent in our recordings.

For imaging in awake mobile mice, restrained at the spinal cord and head level, we used an upright two-photon microscope (Sutter Instrument Company) equipped with an 8-kHz resonant scanner (Cambridge Technology, Inc.), a pulsed femtosecond Ti:Sapphire laser (Chameleon Vision II, Coherent), a T565LPXR beamsplitter (Chroma), ET525/70M and ET605/70M emission filters (Chroma), two GaAsP photomultiplier tubes (H10770PA-40 MOD; Hamamatsu), and either a 20x 1.0-NA (XLUMPlanFLN; Olympus) or 16x 0.8-NA water-immersion objective (CFI75; Nikon). Custom modifications to this microscope included the integration of an adaptive focus control unit (WDI), allowing real-time measurement and correction of axial distance changes between microscope objective and optical window with sub-micrometer precision (18). Typical average power used for imaging lamina I and II of Thy1-eYFP-H or SOM-tdTomato mice was 10-25 mW. 20-30 mW was used for imaging of AAV-injected animals expressing GCaMP6f in either dorsal horn neurons or astrocytes. Image resolution was 256 x 512 pixels (frame rate, 61.8 fps) or 512 x 512 pixels (frame rate, 30.9 fps).

Imaging of the same dorsal horn cells with two- and miniaturized one-photon microscopy on a given day (Figure 2.3 and 2.13), and repeated imaging of the same cells over multiple days (Figure 2.16) was achieved by precisely aligning the animal under the microscope using characteristic surface blood vessels as reference structures, similar to our previous work (52).

In vivo image data processing and analysis

One-photon images from freely behaving mice were cropped to fluorescently labeled, central FOV areas. Within-frame distortions in cropped images were typically small and therefore not corrected. Full-frame lateral motion artifacts were corrected using TurboReg (15), or manually.

Motion-corrected calcium imaging data was analyzed using custom MATLAB software based on principal and independent component analysis (PCA/ICA) (20), which automatically computes region of interest (ROI) spatial filters and minimizes signal crosstalk. PCA/ICA analysis was supplemented by manual ROI analysis to include cells that were apparently missed by the algorithm. For manually selected cells to be included in analysis, these cells had to exhibit a ≥50% ΔF/F calcium transient at least once during the entire imaging session, which included presentations of different stimuli or stimulus intensities under anesthetized and awake conditions. ROI analysis was done in ImageJ.

Two-photon imaging data from awake mobile mice was corrected for lateral motion artifacts using TurboReg (15). Motion-corrected calcium imaging data was analyzed using MATLAB-based PCA/ICA or ImageJ-based ROI analysis, as described above.

To identify calcium transients within extracted GCaMP6f activity traces we computationally searched for local maxima with a) a peak amplitude more than two standard deviations (2σ) from the trace's baseline, b) ≥0.2 s surrounding the peak having a minimum intensity >2σ, and c) ≥0.2 s separation between transients. For astrocyte calcium excitations above 2σ with two or more peaks, we counted each peak as separate transient if the amplitude between peaks fell below the half maximum of the lowest peak for ≥0.2 s. Calcium transient occurrence was set to the temporal midpoint in the rise to peak fluorescence from the most recent trough, approximating a time midway in the corresponding calcium spike.

For neurons, calcium transients were considered stimulus-evoked if they occurred within 1 s after stimulus delivery and were not associated with measureable locomotor activity of the animal, as determined by behavioral video. Calcium transients were considered movement-evoked if they occurred in the absence of a deliberate stimulus and within 400 ms of measureable bodily movement.

For astrocytes, calcium transients were considered stimulus-evoked if they occurred during stimulus delivery. Calcium transients were considered movement-evoked if they occurred

in the absence of a deliberate stimulus and during running, as determined by behavioral video or encoder data. Calcium transients were considered a large-scale coordinated event if a) at least 7 ROIs within the field of view had a peak amplitude more than two standard deviations (2σ) from the trace's baseline, and b) during a ±1.5 s time window surrounding this event at least 15 ROIs had a mean intensity $>2\sigma$ for ≥0.2 s. Large-scale events were considered stimulus-evoked if they occurred within 7 s after stimulus delivery, and running-evoked if they occurred in the absence of a deliberate stimulus and within 7 s after running onset. When stimulus and locomotor activity coincided, we calculated the latency to onset and offset to determine transients' functional relationship (Figure 2.15f-g).

Behavioral video data from freely moving mice was manually scored for periods of rest, movement, grooming, or other forms of animal activity. Encoder data from restrained mice on a spherical treadmill was quantified as previously described (4, 20).

To determine imaging depth and spatial resolution of our miniaturized one-photon microscopes we recorded from the same spinal cord region in fluorescent reporter (Thy1-eYFP-H or SOM-tdTomato) mice using two- and miniaturized one-photon microscopy. Maximum imaging depth was defined as the sub-dural focal depth up to which the same cellular structures could be identified in fluorescence images acquired with both imaging modalities (Figure 2.3). Spatial resolution was determined by comparing full-width at half maximum (FWHM) from line profiles through the same cellular structures recorded with both imaging modalities (Figure 2.4).

Axial tissue movement was estimated by first recording two- or one-photon images at different sub-dural focal positions in the anesthetized animal (typically 40 images acquired at 1 μm axial spacing). Focal shifts in optical recordings from the behaving animal were then determined by comparing cellular structures (e.g., FWHM of cell bodies or processes) in the time-lapse images with the same structures in the reference z-stack acquired under anesthesia.

Analog and video data processing and analysis

Cutaneous stimuli were applied to the base of the animal's tail (at ~5 mm distance from the animal's dense coat hair). Pressure stimuli (30, 70, 130, 220, 400, 600 or 800 g) were applied using a rodent pincher system (2450, IITC Life Science, Inc.). The order in which these stimuli were applied was randomized. Inter-stimulus interval was typically ≥60 s. Based on previous work (33, 53, 54), three pressure categories were defined for analysis: Low- (P = 30-70 g), medium- (P = 130-220 g), and high-amplitude pressure (P = 400-800 g). Pressure sensor output was recorded using MCS software (Sutter Instrument Company; sampling rate, 1 kHz). Brief air puff stimuli were applied using a compressed air canister with its nozzle pointing at the target area and away from coat hair (nozzle tip-to-target area distance, ~15 mm). Air puff application and mouse behavior was recorded on video camera (Stingray F-033, Allied Vision Technologies; 30 or 60 fps). For mice focally restrained on a spherical treadmill running speed was also tracked using an optical encoder (E7PD-720-118, US Digital). The order in which different stimuli were applied was randomized. Inter-stimulus interval was typically ≥60 s.

To synchronize one- or two-photon fluorescence imaging data with video data we placed a 680 nm or 870 nm LED, triggered from the miniaturized microscope's light source or two-photon microscope's shutter transistor-transistor logic (TTL) signal, within the video camera's field of view. Video data was cropped to the LED-on period. One-photon imaging and analog data was synchronized by recording the on-off TTL signal of the miniaturized microscope's light source together with the analog output signal from the pressure sensor in MCS. The pincher trace was then cropped to the light source-on period. Two-photon imaging and pressure sensor and/or encoder data was synchronously recorded in MCS.

Pressure sensor data was recorded at 4 Hz (limited by the pressure meter and limiting measurement accuracy of response latency in Figure 2.8d). Pressure stimulus onset was defined as the point at which the smoothed pressure trace exceeded P = 10 g. This definition was used to calculate calcium transient latency shown in Figure 2.8d, 2.15f, 2.15g. Pressure traces were

quantified with respect to stimulus amplitude and duration using custom MATLAB (Mathworks) routines. Only data for which peak stimulus amplitude remained stable (within 10, 30 or 70 g for low-, medium- or high-amplitude stimuli, respectively) for at least 50% of the pinch duration, defined as full-width at half-maximum, was included in analysis (Figure 2.8e-f, 2.14e-f). Likewise, only data for which pinch duration was similar (typically within ±1.25 s of the target duration; within ±20% of the short target duration shown in Figure 2.12d) for a given peak stimulus amplitude was included in analysis (Figure 2.9a-d, 2.11c-d, 2.12c-d, 2.14d, 2.15c-g).

Encoder data was recorded at 1 kHz. Encoder traces were smoothed using a sliding average (window size, 0.4 s). Locomotion onset or offset was defined as the point at which the smoothed running speed exceeded or fell below 10 mm per second. Encoder traces were analyzed with respect to maximum and average running speed, running duration and frequency of running.

Behavioral data processing and analysis

To quantify locomotor performance of freely behaving mice, animals were placed on a motorized linear treadmill (Exer Gait XL, Columbus Instruments). Mouse behavior was recorded using two video cameras, one monitoring the animal's footsteps from below the translucent treadmill belt (at 100 fps) and the other monitoring the animal's vertical activity (at 60 fps) through a transparent side wall parallel to the belt's movement direction. Hind limb stride length was extracted from footstep recordings using TreadScan (Clever Sys Inc.). Maximum running speed was defined as the belt speed up to which animals were able to avoid end wall collisions during the 1-2 min measurement period, during which belt speed was gradually and manually increased. Mice were habituated to the linear treadmill prior to recordings.

To quantify locomotor performance of awake mobile mice, focally restrained animals were placed on a spherical treadmill for ~5 min for each restraint type (head restraint, spinal cord restraint, or combined spinal cord and head restraint). The order in which animals were subjected to the three different restraint types was randomized. Animals were allowed to rest for at least 10

min between recordings for each restraint type (10 sessions over 3 consecutive days). Collected encoder data was analyzed with regard to rest and running periods, maximum and average running speed using custom MATLAB (Mathworks) routines. Mice were habituated to focal restraint on the spherical treadmill for 5 consecutive days prior to recordings.

Immunofluorescence

Mice were euthanized in their home cage at different time points after viral vector injection, spinal imaging chamber implantation, or in vivo imaging using CO_2 asphyxiation at a 20% fill rate, in accordance with IACUC guidelines. Animals were then quickly transcardially perfused with 10% sucrose followed by 4% paraformaldehyde (PFA). Spinal cord tissue between the L1-L5 vertebra level was carefully extracted and allowed to incubate in 4% PFA overnight at 8 °C. Fixed tissue was thoroughly washed on a plate shaker with 1x phosphate buffered saline (PBS) three times over ~1 hour.

Perfused and PBS-washed tissue was then sectioned at 50 μm using a Leica VT1000s model vibratome. Immunostaining was performed on floating coronal sections using standard techniques. Primary antibodies included GFAP 1:250 (Millipore Cat. #MAB3402). Secondary antibodies (1:100) included Alexa Fluor 633 goat anti-mouse (Life Technologies Cat. #A21052).

Confocal imaging of stained tissue sections was performed on a Zeiss LSM 780. Two channel tiled z-stacks were acquired to produce images of whole tissue sections (laser lines: 488 nm, 633 nm). Image size was 1024 x 1024 pixels stitched into 3-5 x 3-5 tiles (frame scanning; pixel dwell time, 1.58 μs; average, 2 frames). Images were taken with an Olympus 20x 0.8-NA air-matched objective.

Images were processed and analyzed using ImageJ software.

Statistical analysis

Data was analyzed and plotted using MATLAB, Excel, or Prism software. All data are

represented as mean ± SEM. Group sample sizes were chosen based on previous studies and/or power analysis. The following convention was used to indicate p values: “n.s.” indicates $p > 0.05$, “*” indicates $0.01 < p \leq 0.05$, “**” indicates $0.001 < p \leq 0.01$, “***” indicates $0.0001 < p \leq 0.001$, and “****” indicates $p \leq 0.0001$.

Acknowledgements

This chapter is an adaptation of Sekiguchi K.J., Shekhtmeyster P., Merten K., Arena A., Cook D., Hoffman E., Ngo A. and Nimmerjahn A.. Imaging large-scale cellular activity in spinal cord of freely behaving mice. Nat. Commun.. The dissertation author was a primary author.

I thank Ariana Lorenzana and Binhai Zheng for help with initial spinal cord surgeries; Jovanny Bourane and Martyn Goulding for generously providing SOM-tdTomato mice; Martyn Goulding and Fred H. Gage for manuscript feedback; Joseph Chambers for mouse colony management; the Waitt Advanced Biophotonics Center and Behavioral Testing Core facilities for help with in vitro microscopy and behavioral testing, respectively, and all members of the Nimmerjahn lab for critical feedback on select data; the GENIE Program at the Janelia Research Campus/Howard Hughes Medical Institute for GCaMP6 and viral vector access through the Penn Vector Core.

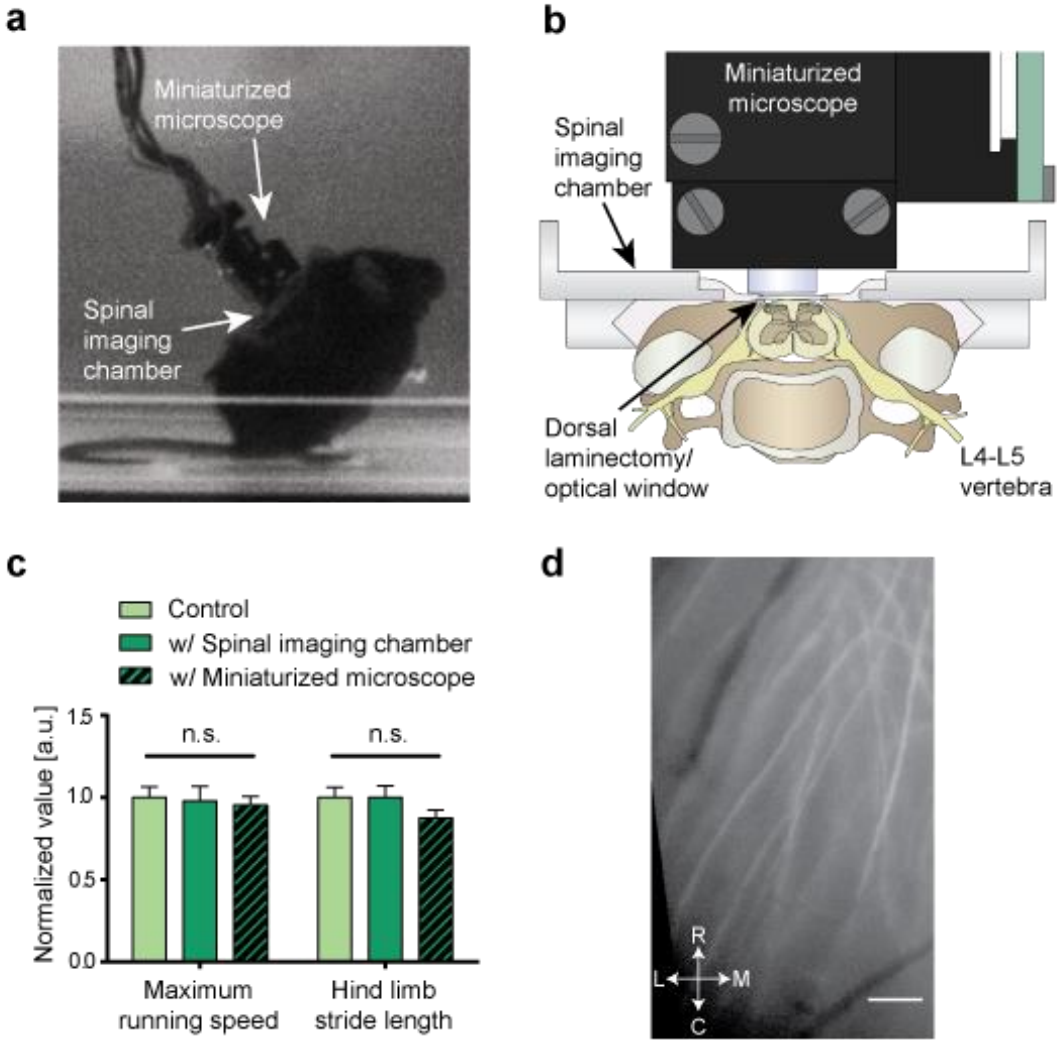

Figure 2.1 Cellular resolution imaging in spinal cord of freely behaving mice. (a) Image of a mouse with a custom miniaturized one-photon microscope mounted over a spinal imaging chamber implanted at the lumbar level. Mouse behavior on a motorized linear treadmill was videotaped. Video and imaging data was synchronized prior to analysis. **(b)** Schematic showing the implanted imaging chamber and mounted miniaturized one-photon microscope in cross-section. The chamber was implanted at the lumbar level. **(c)** Population data showing maximum running speed and hind limb stride length on the motorized linear treadmill for mice implanted with a spinal imaging chamber (dark green), the same mice with a miniaturized microscope mounted over the imaging chamber (patterned dark green), or the same mice before the surgery (light green). Behavioral measurements of mice with a spinal imaging chamber were taken one day after implantation. **(d)** Fluorescence image showing yellow fluorescent protein-expressing axons in dorsal spinal cord of a Thy1-eYFP-H mouse acquired with the miniaturized one-photon microscope prior to terminating anesthesia. The subregion image is an average of 800 frames acquired at 45 fps. Medio-lateral and rostro-caudal direction is indicated. Scale bar, 50 μm. Data are represented as mean ± SEM. (c) shows comparison between the same mice before and after surgery; one-way repeated measures ANOVA ($p \geq 0.05$; N = 5 mice per group).

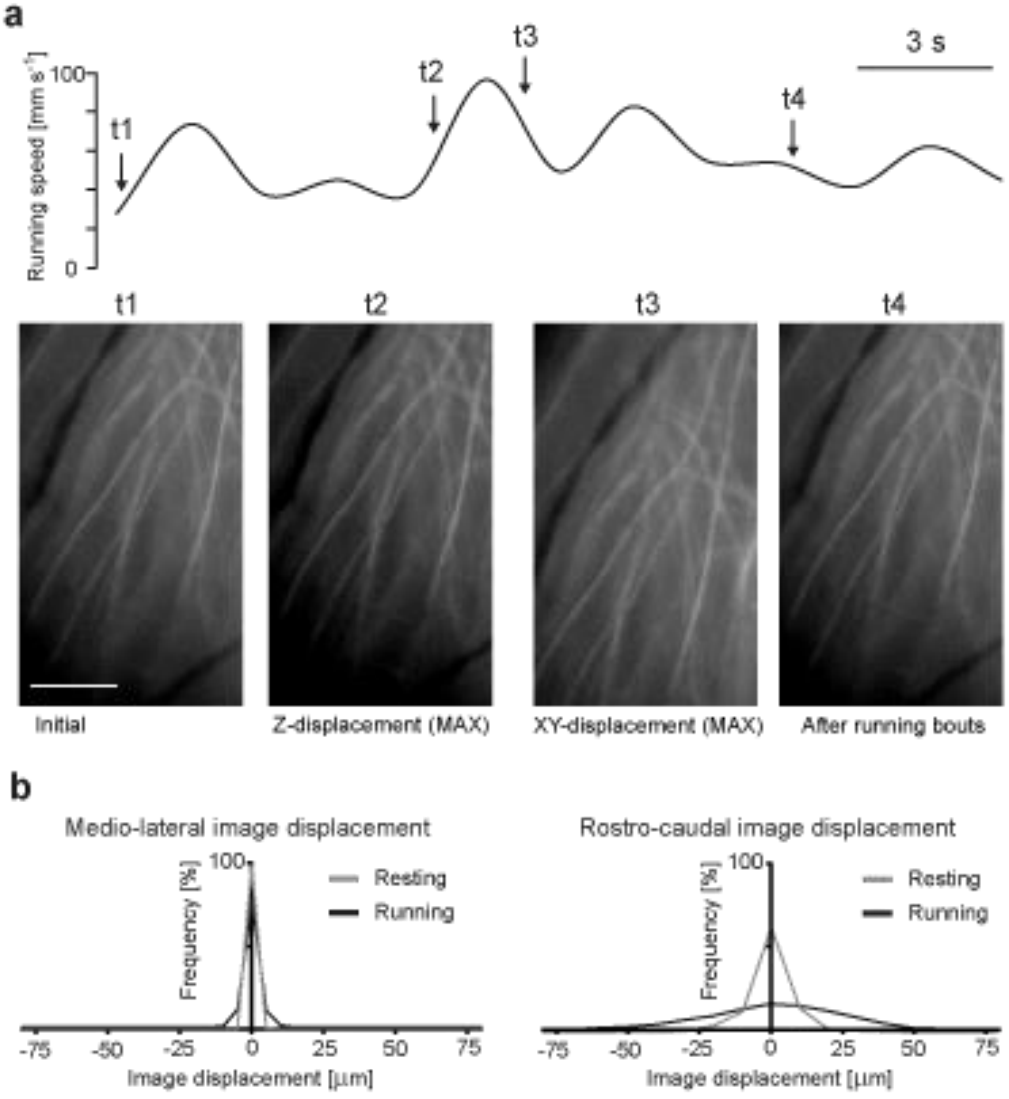

Figure 2.2 Image displacement during cellular resolution imaging in spinal cord of freely behaving mice. (a) *Top*, mouse treadmill running speed (black trace) over a 20-second recording period. *Bottom*, subregion images showing the initial frame (t1) and frames with maximum image displacement (t2, t3) during the awake recording period. Image displacement was transitory (t4) and mainly occurred in rostro-caudal direction. Scale bars, 3s (top) and 100 µm (bottom). **(b)** Population data showing probability distribution of medio-lateral (left) and rostro-caudal (right) image displacements during rest (gray) and running (black). Dorso-ventral image displacements were ≤5 µm (see Methods).

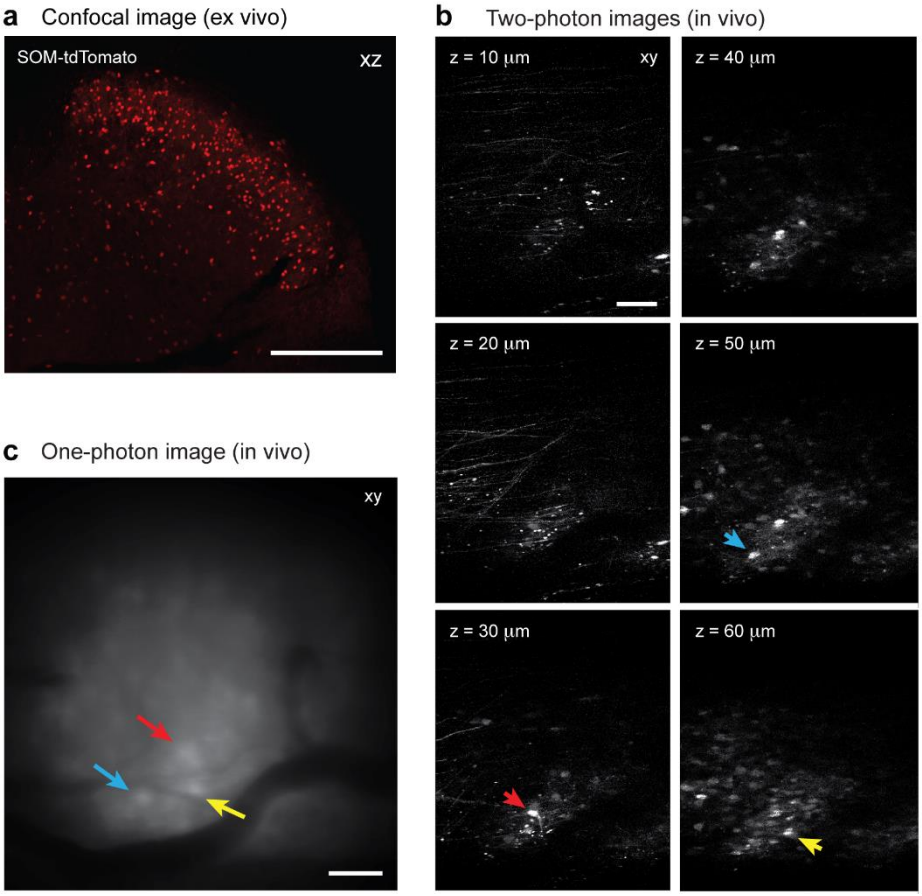

Figure 2.3 Dorsal horn imaging depth with miniaturized one-photon microscopy. (**a**) Confocal image showing dorsal horn cells in a coronal (xz) spinal cord section from a SOM-tdTomato mouse. tdTomato expression in this mouse line is restricted to somatostatin (SOM) lineage neurons, whose cell bodies are located primarily in lamina II and below. Scale bar, 200 μm. (**b**) Two-photon images from a z-stack showing tdTomato-expressing cells in an anesthetized SOM-tdTomato mouse. Focal depth (z) below the dura is indicated in the transverse (xy) images. Scale bar, 50 μm. (**c**) One-photon image taken with a miniaturized microscope from the same dorsal horn region shown in **b**. Three tdTomato-expressing cells that appear in both one- and two-photon images are indicated (blue, red, and yellow arrows). The one-photon volume image captures cells located at different focal depth, allowing their simultaneous recording. Scale bar, 50 μm.

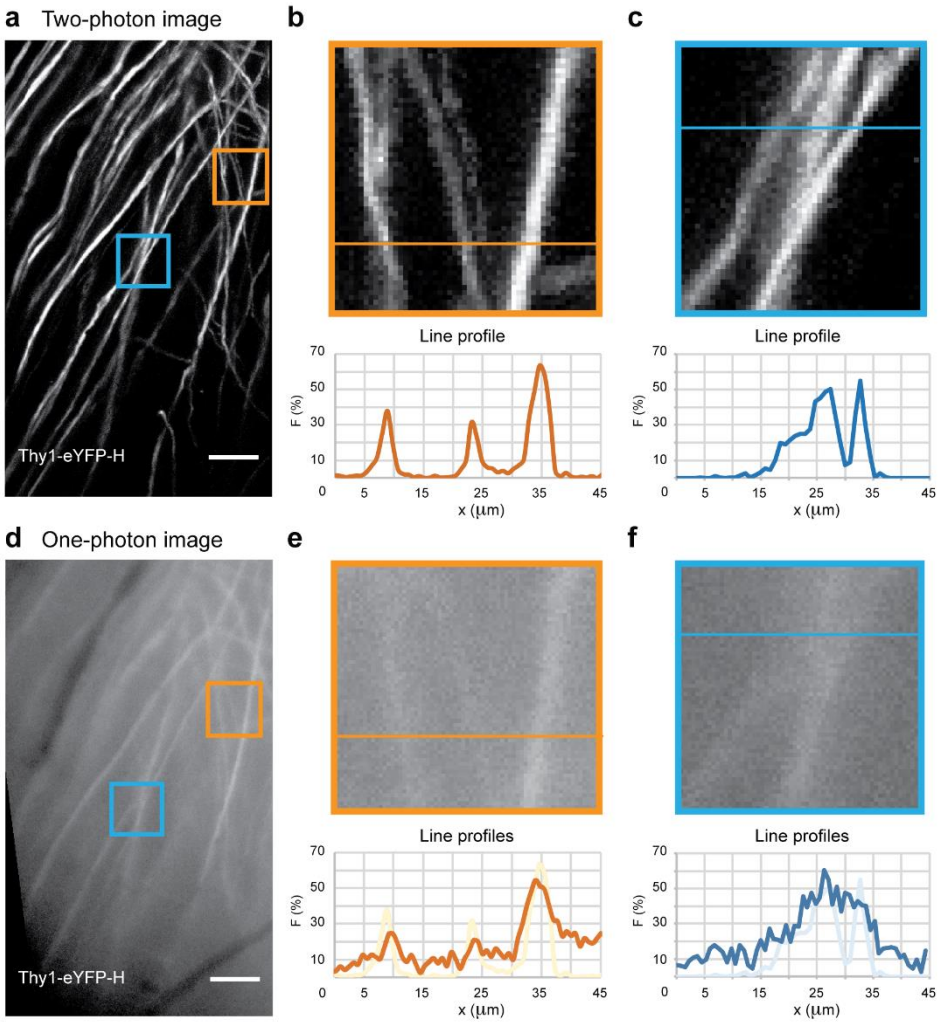

Figure 2.4 Spatial resolution with miniaturized one-photon microscopy. (**a**) Maximum-intensity projection image from a two-photon z-stack (depth, 3-27 μm below the dura; axial spacing, 1 μm; frame average, 8) showing sparsely labeled axons in dorsal spinal cord of an anesthetized Thy1-eYFP-H mouse. Two regions of interest (ROIs; orange and blue) are indicated. Scale bar, 50 μm. (**b**) *Top*, orange boxed region in **a** shown at higher magnification. *Bottom*, relative fluorescence intensity profile along the orange horizontal line indicated in the magnified image. (**c**) *Top*, blue boxed region in **a** shown at higher magnification. *Bottom*, relative fluorescence intensity profile along the blue horizontal line indicated in the magnified image. (**d**) One-photon volume image (same image as in Figure 2.1d) showing the same spinal cord region as in **a**. The same two ROIs as in **b** were analyzed. Scale bar, 50 μm. (**e**) *Top*, orange boxed region in **d** shown at higher magnification. *Bottom*, relative fluorescence intensity profile along the orange horizontal line indicated in the magnified image. The corresponding two-photon line profile is overlaid in light orange. (**f**) *Top*, blue boxed region in **d** shown at higher magnification. *Bottom*, relative fluorescence intensity profile along the blue horizontal line indicated in the magnified image. The corresponding two-photon line profile is overlaid in light blue. Closely spaced axons or axon bundles cannot be resolved with miniaturized one-photon microscopy.

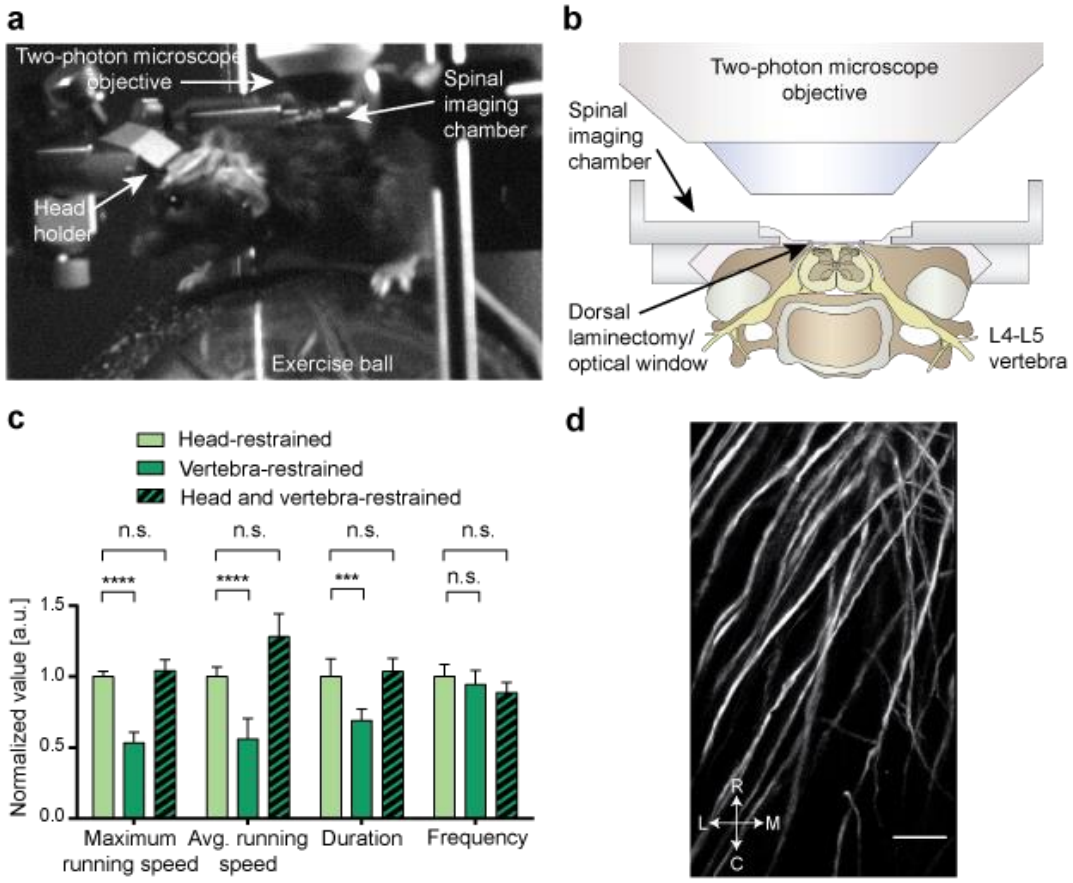

Figure 2.5 Cellular resolution imaging in spinal cord of awake mobile mice. (a) Image of a mouse focally restrained at the level of the spinal cord and head, and placed on a spherical treadmill under a two-photon microscope. **(b)** Schematic showing the implanted imaging chamber and two-photon microscope objective in cross-section. The chamber was implanted at the L4-L5 vertebra level. **(c)** Population data showing maximum and average running speed, and average running duration and frequency on the spherical treadmill for mice restrained at the lumbar vertebra level (dark green), the same mice restrained at the lumbar vertebra level and head (patterned dark green), or only at the head (light green). Measurements under the three restraint conditions were randomized. Behavioral measurements were taken seven days after chamber implantation and after five days of habituation. **(d)** Fluorescence image showing yellow fluorescent protein-expressing axons in dorsal spinal cord of the same Thy1-eYFP-H mouse shown in Fig. 1d, but acquired with a two-photon microscope. (same image as in Figure 2.4a) The image is a maximum intensity projection through a stack of 25 images acquired under anesthesia (axial spacing, 1μm; frame average, 8; frame rate, 30.9 fps). Medio-lateral and rostro-caudal direction is indicated. Scale bar, 50 μm. Data are represented as mean ± SEM. (c) shows comparison between mice under different restrained conditions; one-way repeated measures ANOVA, N = 6 mice per group ($p < 0.05$ for comparison between "Head-restrained" and "Vertebra-restrained" groups under "Maximum running speed", "Avg. running speed" and "Duration"; $p \geq 0.05$ for all other comparisons)

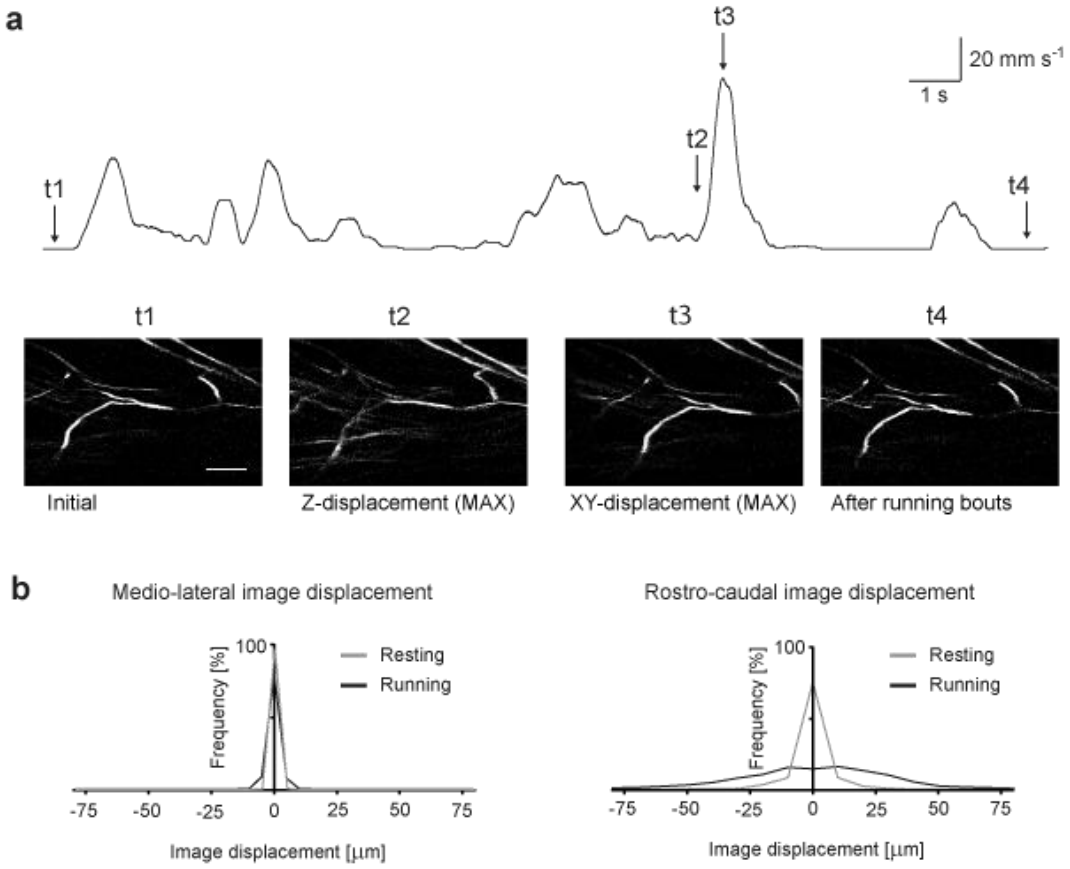

Figure 2.6 Image displacement during cellular resolution imaging in spinal cord of awake mobile mice. (e) *Top*, mouse treadmill running speed (black trace) during a 20-second recording period. *Bottom*, images showing the initial frame (t1) and frames with maximum image displacement (t2, t3) during the awake recording period. Image displacement was transitory (t4) and occurred mainly in rostro-caudal direction. Scale bars, 20 mm per s and 1s (top), and 50 μm (bottom). **(f)** Population data showing probability distribution of medio-lateral (left) and rostro-caudal (right) image displacements during rest (gray) and running (black). Axial displacements were typically ≤5 μm (see Methods). Mice were habituated to spinal cord and head restraint for typically five days prior to optical measurements.

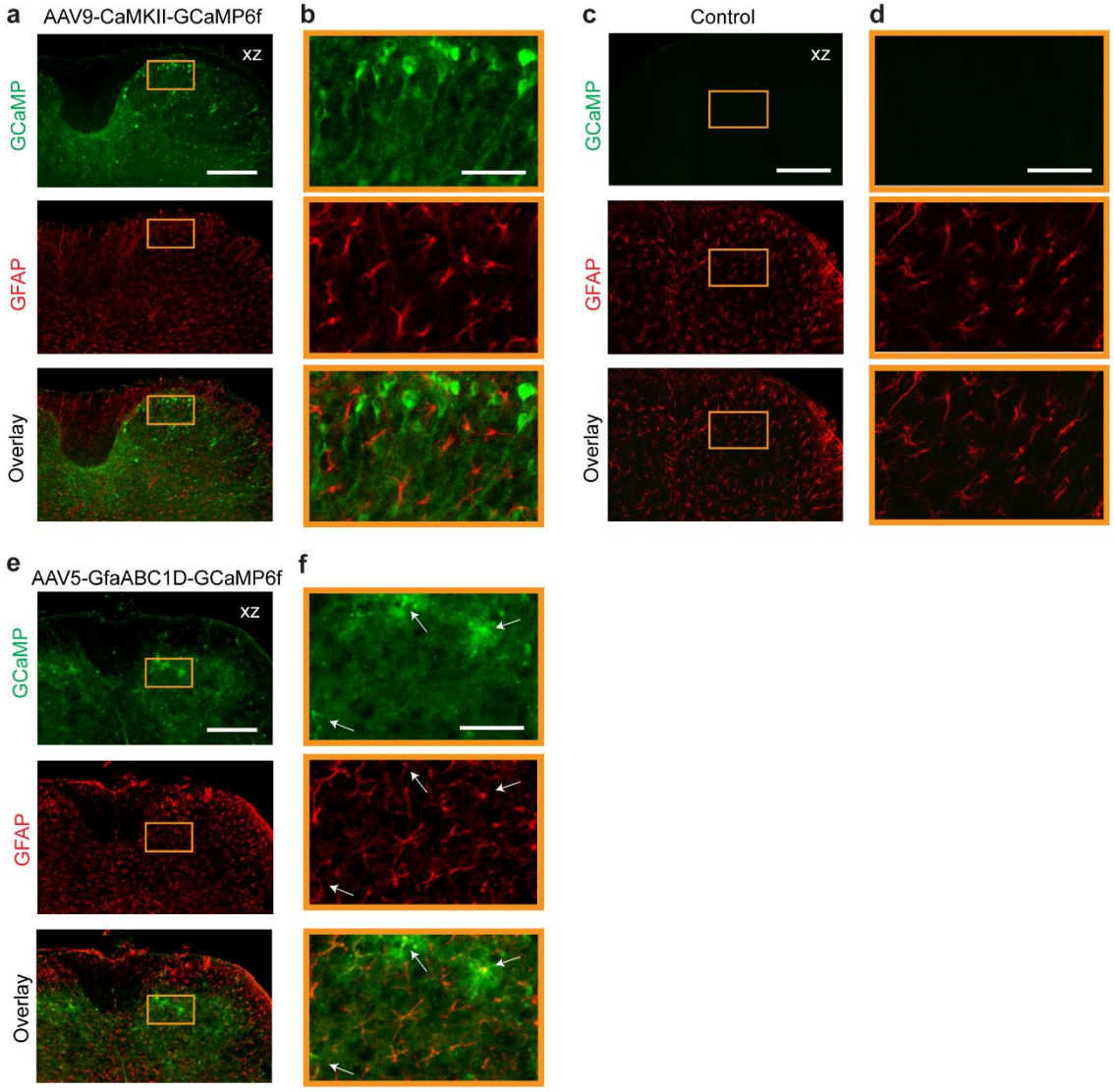

Figure 2.7 AAV-mediated labeling of spinal cord neurons and astrocytes. (**a**) *Top*, confocal image showing GCaMP6-transduced dorsal horn cells in a coronal (xz) lumbar (L4-L5 vertebra) level section from a wild type mouse 14 days after AAV9-CaMKII-GCaMP6f injection, and immediately after spinal cord window implantation and *in vivo* imaging. *Center*, glial fibrillary acidic protein (GFAP) co-staining. *Bottom*, overlay image. Scale bar, 150 μm. (**b**) Magnified images of the boxed regions (orange) shown in **a**. Scale bar, 50 μm. (**c**) Confocal images from a coronal L1-L2 vertebra level control section obtained from the same mouse shown in **a**. *Top*, image showing lack of GCaMP6-transduction. *Center*, GFAP staining. *Bottom*, overlay image. Scale bar, 150 μm. (**d**) Magnified images of the boxed regions (orange) shown in **c**. Scale bar, 50 μm. (**e**) Confocal images from a wild type mouse 21 days after AAV5-GfaABC1D-GCaMP6f injection, and immediately after spinal cord window implantation and *in vivo* imaging. GCaMP6 staining (green) and GFAP co-staining (red) are shown atop the overlay image. Scale bar, 150 μm. (**f**) Magnified images of the boxed regions (orange) shown in **e**. A subset of co-stained cells isindicated. Scale bar, 50 μm.

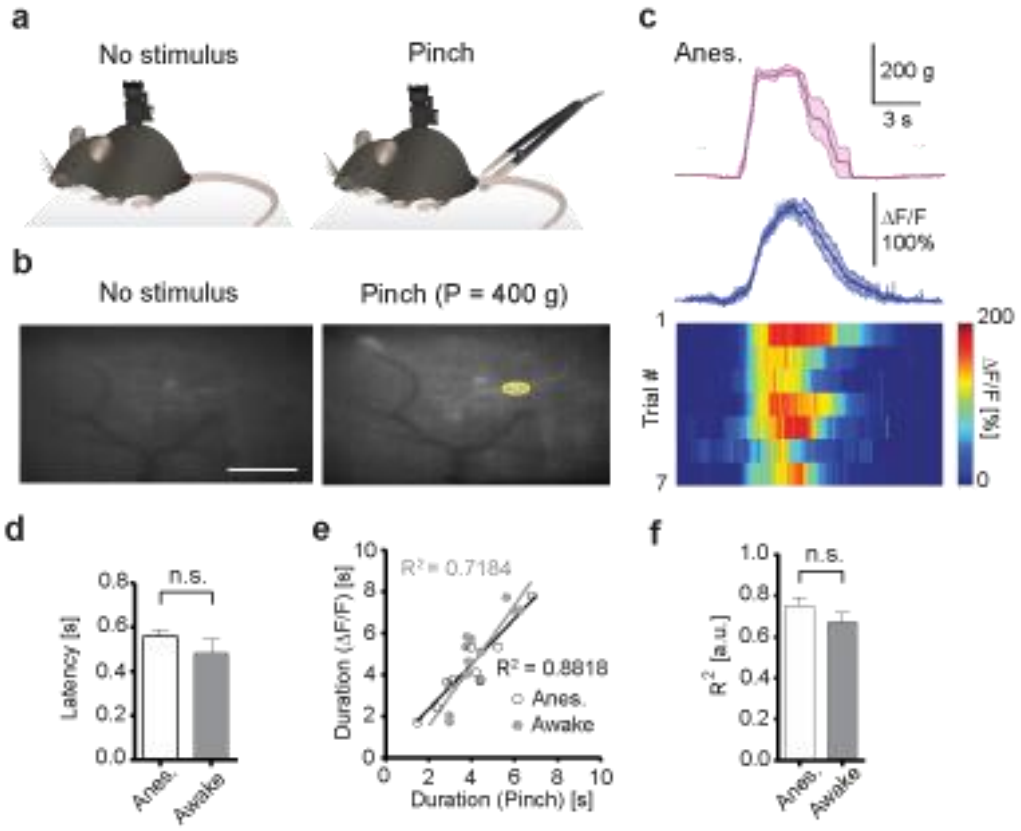

Figure 2.8 Dorsal horn neurons encode sensory information at the single cell level. (a) Schematic of experimental approach. Calcium spiking in dorsal horn neurons of anesthetized and awake mice injected with AAV9-CaMKII-GCaMP6f was recorded during rest (left) and following cutaneous stimulation with a rodent pincher applied to the base of the animal's tail (right). **(b)** Example fluorescence images showing transduced cells during rest (left) and in response to tail pinch (right; P = 400 g) under anesthesia. A somatic region of interest (ROI) is indicated (yellow). Scale bar, 100 μm. **(c)** Pinch-evoked calcium responses in the ROI highlighted in b. *Top*, average trace of applied pinch stimulus. *Center*, average pinch-evoked calcium transient. *Bottom*, individual calcium transients for seven individual trials. **(d)** Population data showing calcium transient latency with respect to pinch onset for anesthetized (white) and awake mice (gray) (see Methods). **(e)** Relationship between pinch and calcium transient duration for a representative dorsal horn neuron under anesthetized (open circles) and awake conditions (closed circles) (P = 220 g). A linear fit to the anesthetized and awake data (black and gray line, respectively) is shown. **(f)** Population data showing that calcium responses in dorsal horn neurons linearly encoded pinch duration in anesthetized and awake mice. Analysis included only cells that responded under both anesthetized and awake conditions. Data are represented as mean ± SEM. (d) shows unpaired t-test with Welch's correction, n = 43 cells for "Anes." and n = 59 cells for "Awake" in N = 4 mice per group, $p \geq 0.05$. (f) shows unpaired t-test with Welch's correction, n = 38 cells in N = 4 mice per group, $p \geq 0.05$.

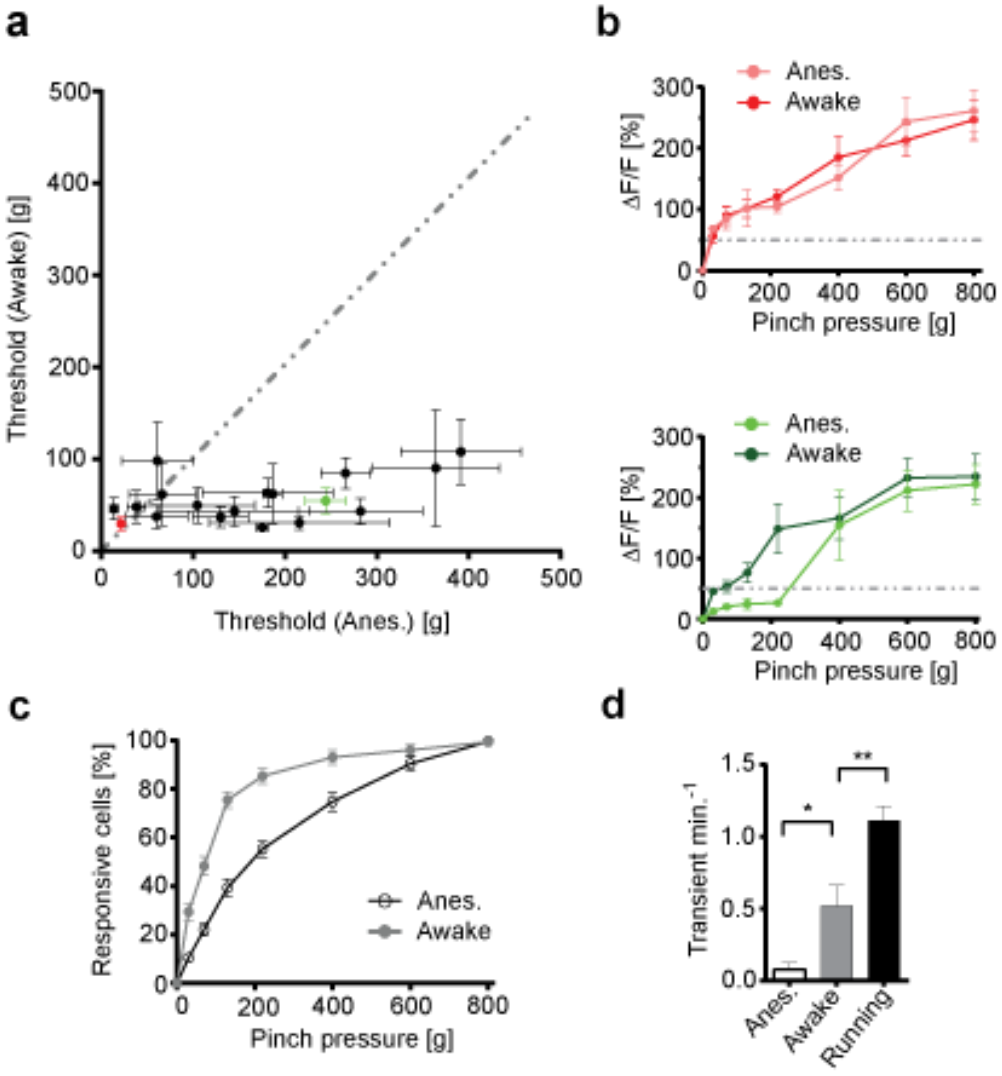

Figure 2.9 Dorsal horn neurons are potently suppressed with anesthesia. (a) Population data showing the responsiveness of individual dorsal horn neurons under anesthetized and awake conditions. **(b)** Relationship between pinch pressure and calcium transient amplitude for the two example neurons indicated in a (red and green). Dotted horizontal line indicates calcium transient amplitude (50% ΔF/F) below which cells were considered unresponsive. **(c)** Population data showing that for a given pinch pressure less neurons responded under anesthetized (open circles) compared to awake conditions (closed circles). **(d)** Population data showing calcium transient frequency in dorsal horn neurons under anesthetized (white), awake resting (gray), and running conditions (black). Data are represented as mean ± SEM. (d) shows unpaired t-test with Welch's correction, n = 28 cells in N = 4 mice per group, $p < 0.05$.

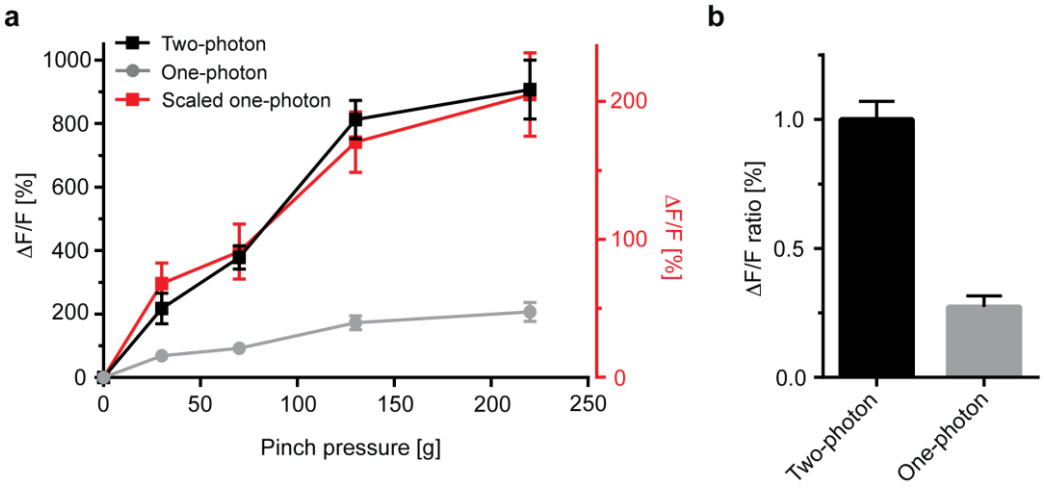

Figure 2.10 Sensitivity with miniaturized one-photon microscopy. (**a**) Average pinch-evoked calcium transient amplitude as a function of pinch pressure for a representative dorsal horn neuron in an anesthetized wild type mouse injected with AAV9-CaMKII-GCaMP6f. The same cell was measured with two- (black; average power, 20 mW) and miniaturized one-photon microscopy (gray; average power, 158 μW per mm^2). While both imaging modalities yield the same functional relationship (red, scaled one-photon trace), small differences in pressure amplitude can be more readily decoded from calcium transients measured with two-photon microscopy in focally restrained mice. (**b**) Population data showing relative calcium transient amplitude of miniaturized one-photon (gray) compared to two-photon microscopy (black). Data are represented as mean ± SEM.

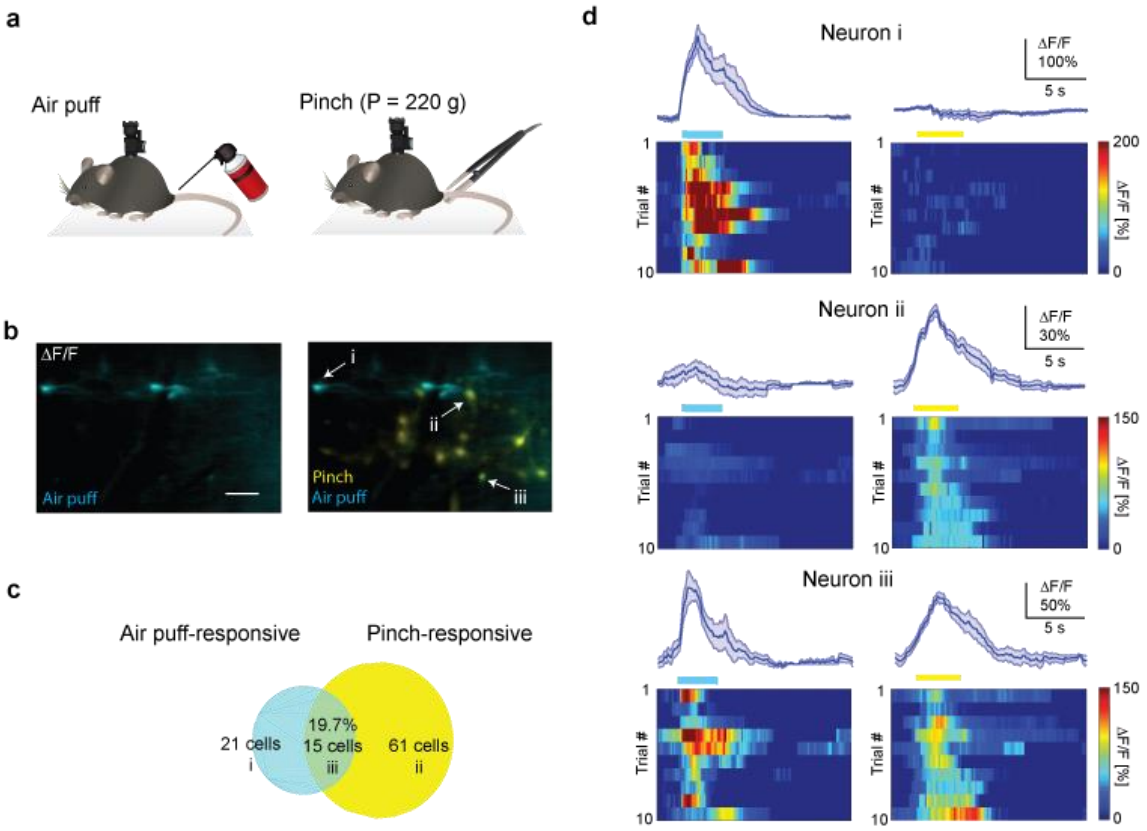

Figure 2.11 Air-puff recruits different subsets of dorsal horn neurons. (a) Schematic of experimental approach. Two different cutaneous stimuli (pinch and air puff) were applied to the base of the animal's tail while monitoring calcium spiking of dorsal horn neurons in wild type mice injected with AAV9-CaMKII-GCaMP6f at the L4-L5 vertebra level under unrestrained awake conditions using a miniaturized microscope. **(b)** Example fluorescence images showing dorsal horn neurons activated by air puff (blue) or pinch (yellow). Overlay is shown on right. Note their different spatial distribution. Three example neurons are indicated. Scale bar, 100 μm. **(c)** Population data showing the number of dorsal horn neurons within the field of view responding to air puff-only, pinch-only, or pinch and air puff. Around 20% of pinch-responsive cells also responded to air puff. **(d)** Average calcium transient (blue trace, top) and single trial responses (bottom) to air puff (left) or pinch (right) for the three example neurons indicated in b. Blue and yellow horizontal bars indicate peripheral stimulus duration. Neuron i responded to air puff-only, neuron ii to pinch-only, and neuron iii to air puff and pinch. Data are represented as mean ± SEM

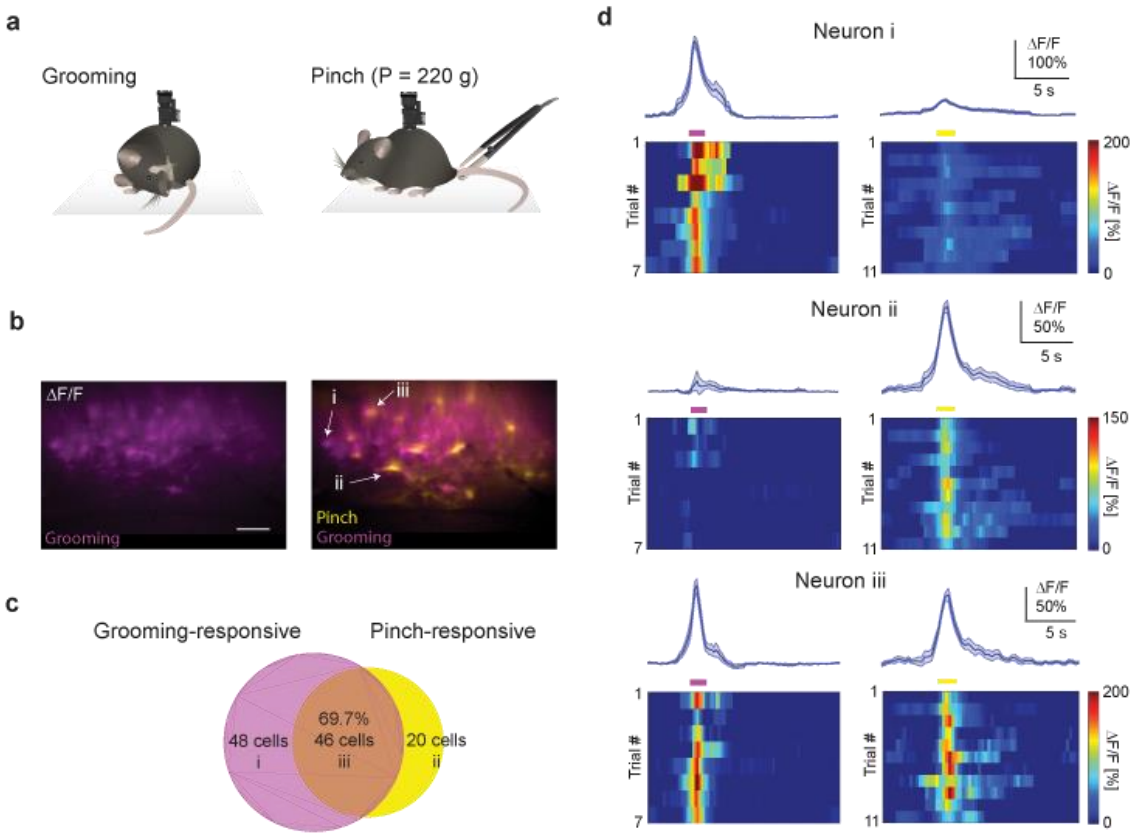

Figure 2.12 Self-initiated hindquarter grooming recruits different subsets of dorsal horn neurons. (a) Schematic of experimental approach. Peripherally evoked calcium spiking in unrestrained awake mice (right) was compared to self-initiated hindquarter grooming near the base of the animal's tail (left). **(b)** Example fluorescence images showing dorsal horn neurons activated by hindquarter grooming (purple) or pinch (yellow). Overlay is shown on right. Note their different spatial distribution. Three example neurons are indicated. Scale bar, 100 μm. **(c)** Population data showing the number of dorsal horn neurons within the field of view responding to grooming-only, pinch-only, or pinch and grooming. Around 70% of pinch-responsive cells also responded to grooming. **(d)** Average calcium transient (blue trace, top) and single trial responses (bottom) to hindquarter grooming (left) or pinch (right) for the three neurons indicated in f. Purple and yellow horizontal bars indicate stimulus duration. Neuron i responded to grooming-only, neuron ii to pinch-only, and neuron iii to grooming and pinch. Data are represented as mean ± SEM.

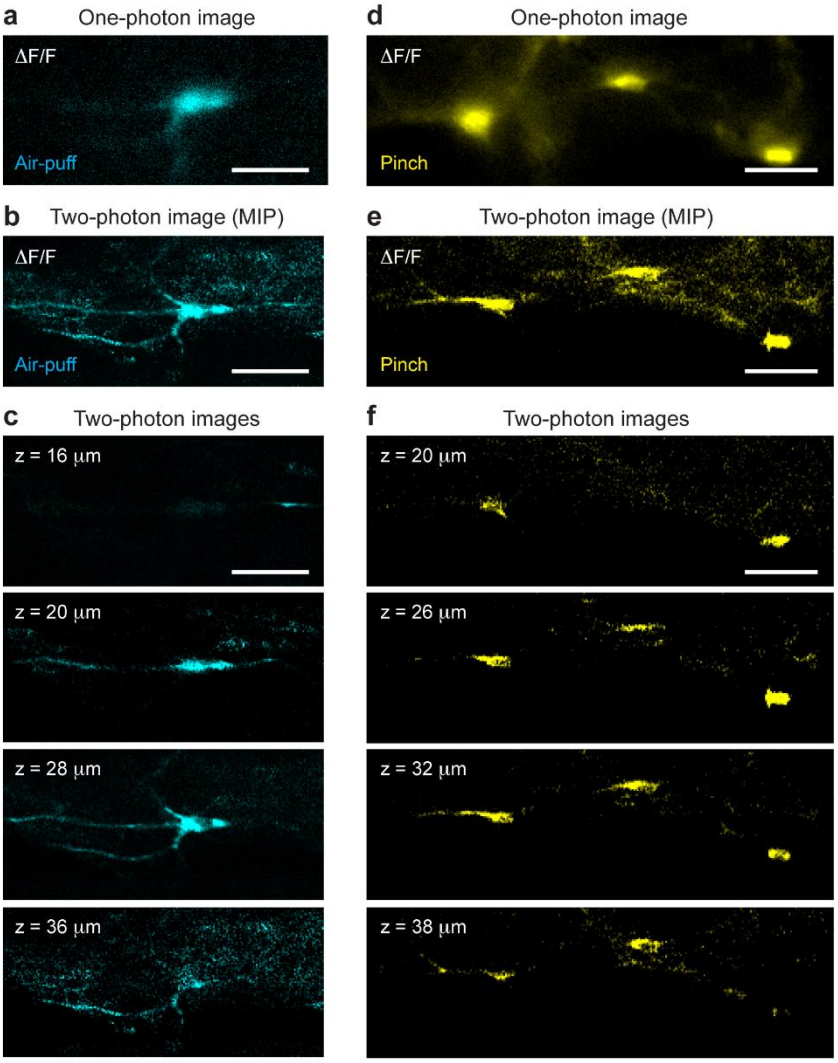

Figure 2.13 Depth determination of peripheral stimulus-responsive dorsal horn neurons recorded with miniaturized one-photon microscopy. (**a**) Fluorescence image showing a dorsal horn neuron in an AAV9-CaMKII-GCaMP6f-injected wild type mouse activated by air puff (blue). Data was recorded in an unrestrained awake mouse using miniaturized one-photon microscopy. Scale bar, 30 μm. (**b**) Maximum-intensity projection (MIP) image from a two-photon z-stack (depth, 16-36 μm below the dura; axial spacing, 2 μm; frame average, 8) showing the same dorsal horn neuron as in **a**. Data was recorded in the awake focally restrained mouse using two-photon microscopy. Similar air puff application was used as during the corresponding one-photon recording. Scale bar, 30 μm. (**c**) Individual two-photon images from the z-stack shown in **b**. Focal depth (z) below the dura is indicated in each image. Scale bar, 30 μm. (**d**) Fluorescence image showing dorsal horn neurons in an AAV9-CaMKII-GCaMP6f-injected wild type mouse activated by pinch (yellow; P = 220 g). Data was recorded in an unrestrained awake mouse using miniaturized one-photon microscopy. Scale bar, 30 μm. (**e**) Maximum-intensity projection (MIP) image from a two-photon z-stack (depth, 20-40 μm below the dura; axial spacing, 2 μm; frame average, 8) showing the same dorsal horn neurons as in **d**. Data was recorded in the awake focally restrained mouse using two-photon microscopy. Comparable pinch parameters were used as during the corresponding one-photon recording. Scale bar, 30 μm. (**f**) Individual two-photon images from the z-stack shown in **e**. Focal depth (z) below the dura is indicated in each image. Scale bar, 30 μm.

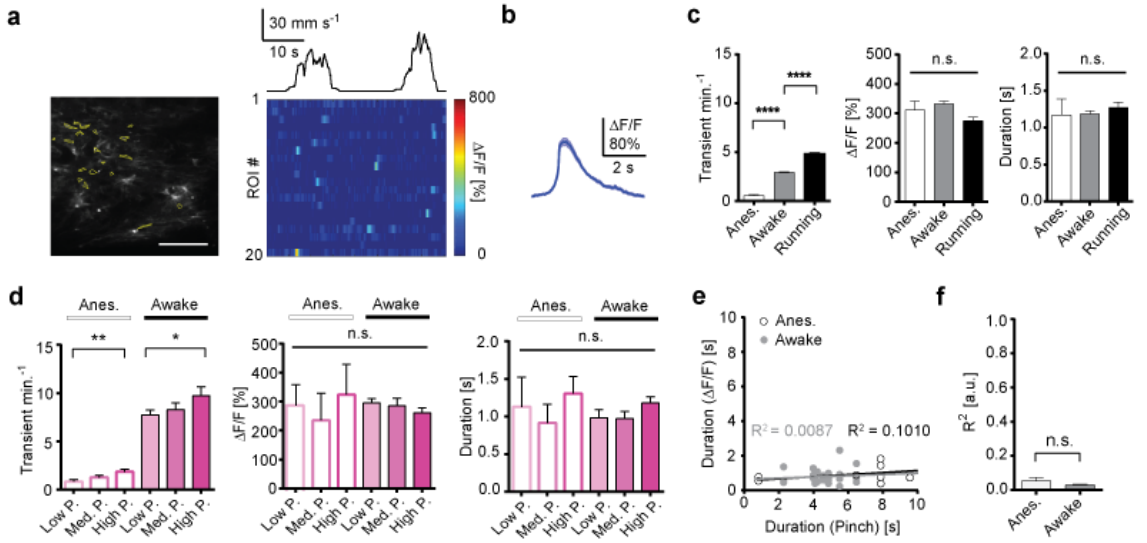

Figure 2.14 Small-scale, unsynchronized calcium transients in dorsal horn astrocytes weakly correlate with sensory information. (a) Left, example fluorescence image showing dorsal horn astrocytes at ~30 µm depth in wild type mice injected with AAV5-GfaABC1D-GCaMP6f. Select astrocyte process regions of interest (ROIs) are indicated (yellow). Right, calcium activity traces of the indicated ROIs during a 45-second recording period in an awake mouse. Mouse running speed (black) is shown on top. Running did not evoke large-scale coordinated calcium excitation. Scale bar, 100 µm. **(b)** Average time course of unsynchronized calcium transients in astrocyte processes. Shown trace is an average of n = 1065 events in N = 4 mice. **(c)** Population data showing calcium transient frequency (left), amplitude (center), and duration (right) of unsynchronized astrocyte calcium transients in anesthetized (white), awake resting (gray), and running mice (black). **(d)** Population data from individual astrocyte processes showing unsynchronized calcium transient frequency (left), amplitude (center), and duration (right) in response to low (pink; P = 30-70 g), medium (magenta; P = 130-220 g), or high-amplitude pinch (purple; P ≥ 400 g) in anesthetized (open bars) or awake mice (solid bars). **(e)** Relationship between pinch and astrocyte calcium transient duration for a representative astrocyte process ROI under anesthetized (open circles) and awake conditions (closed circles) (P = 220 g). A linear fit to the anesthetized and awake data (black and gray line, respectively) is shown. **(f)** Population data showing that individual astrocyte calcium transients do not encode pinch duration in anesthetized or awake mice. Data are represented as mean ± SEM. (c) left panel shows unpaired t-test, n = 84 ROIs in N = 4 mice per group, $p < 0.05$; center and right panels show one-way ANOVA with Tukey-Kramer's multiple comparisons test ($p < 0.05$; n = 84 ROIs in N = 4 mice per group). (d) left panel shows unpaired t-test, n = 84 ROIs in N = 4 mice, $p < 0.05$; center and right panels show one-way ANOVA with Tukey-Kramer's multiple comparisons test ($p \geq 0.05$; n = 84 ROIs in N = 4 mice). (f) shows unpaired t-test, n = 37 ROIs for "Anes." and n = 42 ROIs for "Awake" in N = 4 mice, $p \geq 0.05$.

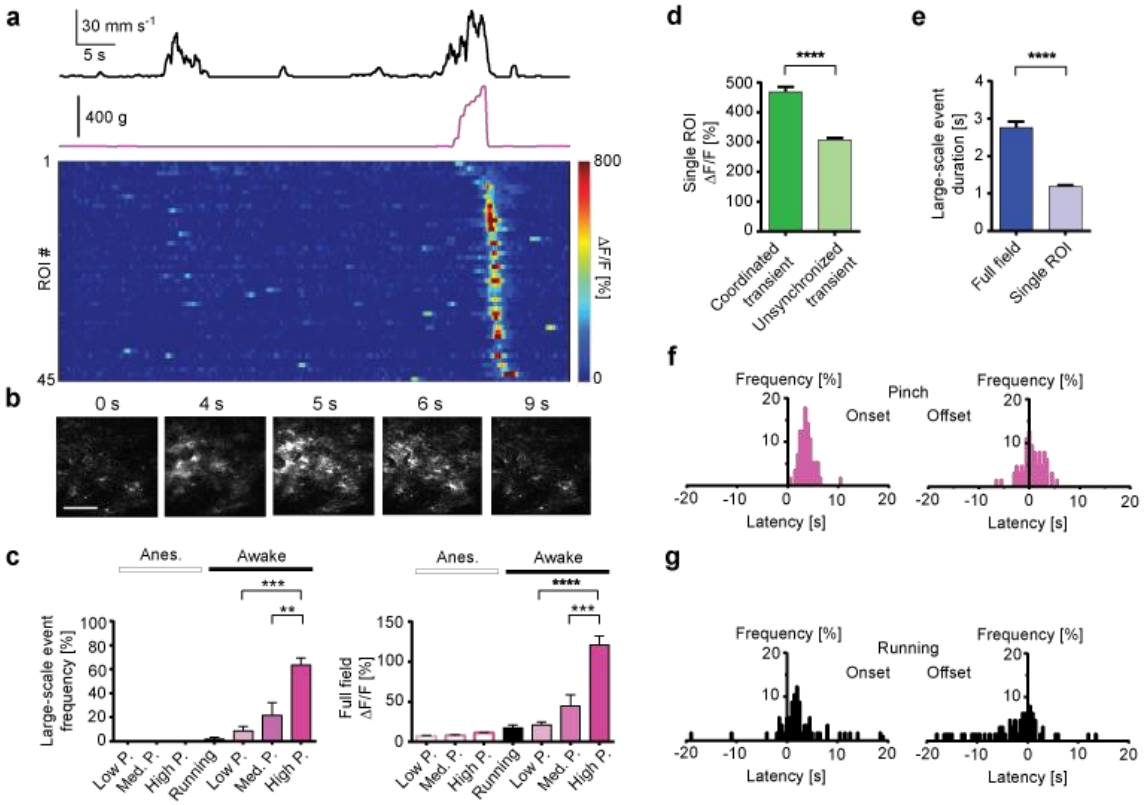

Figure 2.15 Dorsal horn astrocytes show large-scale coordinated calcium excitation to strong but not weak cutaneous input. (a) Calcium activity traces in 45 astrocyte ROIs during a 67-second recording period in an awake mouse. Mouse running speed (black) and tail pinch application (purple) is shown on top. **(b)** Example fluorescence images showing the high-amplitude pinch-evoked coordinated astrocyte calcium excitation of a. Time after pinch onset is indicated. Scale bar, 100 μm. **(c)** Population data showing occurrence frequency (left) of large-scale coordinated calcium events, and average full-field calcium transient amplitude (right), in anesthetized (open bars) or awake mice (solid bars), and in response to low- (pink), medium- (magenta), or high-amplitude pinch (purple). **(d)** Population data showing that the average calcium transient amplitude in individual astrocyte ROIs is larger during large-scale coordinated events compared to unsynchronized calcium transients. **(e)** Population data showing that the duration of large-scale events within the field of view is longer than the duration of individual transients contributing to large-scale events. **(f)** Population data showing latency of large-scale astrocyte calcium events with respect to pinch onset (left) or offset (right). Large-scale events are triggered by pinch onset and have a latency of ~4 s. **(g)** Population data showing latency of large-scale events with respect to the temporally nearest running onset (left) or offset (right). Large-scale events are not triggered by running alone. Data are represented as mean ± SEM. (c) left panel shows paired t-test with Welch's correction, n = 38, 39, 61, 48, 37, 44 or 97 trials (from left to right) in N = 4 mice per group, $p < 0.05$; right panel shows unpaired t-test with Welch's correction; n = 38, 39, 61, 48, 37, 44 or 97 trials (from left to right) in N = 4 mice per group, $p < 0.05$. (d) shows unpaired t-test with Welch's correction, n = 71 ROIs in N = 4 mice per group, $p < 0.05$. (e) shows unpaired t-test, n = 56 for "Full field" and n = 71 for "Single ROI" in N = 4 mice per group, $p < 0.05$

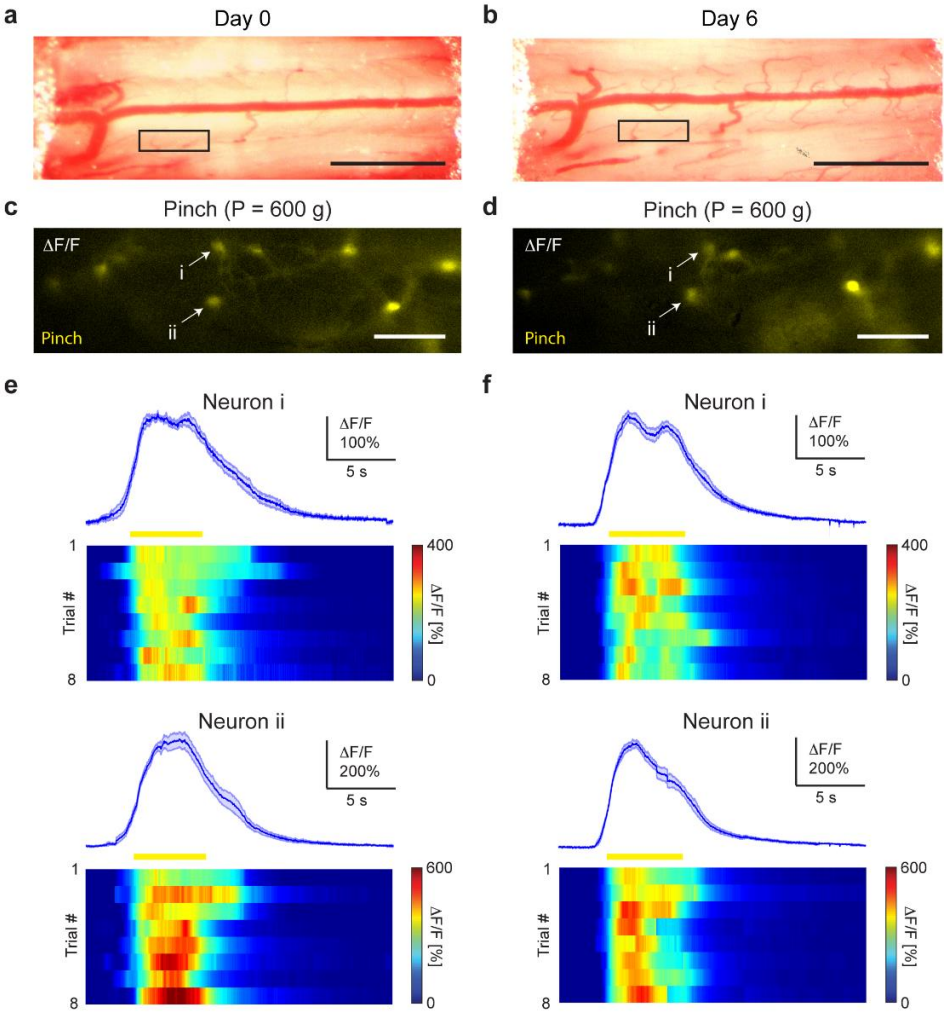

Figure 2.16 Repeated imaging of pinch-evoked calcium activity from dorsal horn neurons. (**a**) Top view onto a lumbar spinal cord window implanted in a wild type mouse that was injected with AAV9-CaMKII-GCaMP6f. The image was taken on the day of surgical preparation (day 0). Virus injection was performed 14 days earlier. Scale bar, 1 mm. (**b**) Top view onto the same spinal cord window shown in **a**, 6 days after surgical preparation. The window remained transparent, allowing repeated imaging. Scale bar, 1 mm. (**c**) Fluorescence image showing dorsal horn neurons activated by pinch under isoflurane anesthesia at day 0 (yellow; P = 600 g). Data was recorded from the boxed region indicated in **a**, using miniaturized one-photon microscopy. Two example neurons are indicated. Scale bar, 100 µm. (**d**) Fluorescence image showing pinch-responsive dorsal horn neurons from the same region as in **c** 6 days after surgical preparation. Comparable pinch parameters were used, and the same two neurons as in **c** are indicated. Many of the same neurons responded similarly to pinch across days. Scale bar, 100 µm. (**e**) Average calcium transient (blue trace, top) and single trial responses (bottom) to pinch at day 0 for the two neurons indicated in **c**. Yellow horizontal bars indicate peripheral stimulus duration. Note the distinct average response amplitude and kinetics of neurons i and ii. (**f**) Average calcium transient (blue trace, top) and single trial responses (bottom) to pinch at day 6 for the same two neurons shown in **e**. Yellow horizontal bars indicate peripheral stimulus duration. Average response amplitude and kinetics for neurons i and ii was similar across days using comparable pinch parameters. Data are represented at mean ± SEM

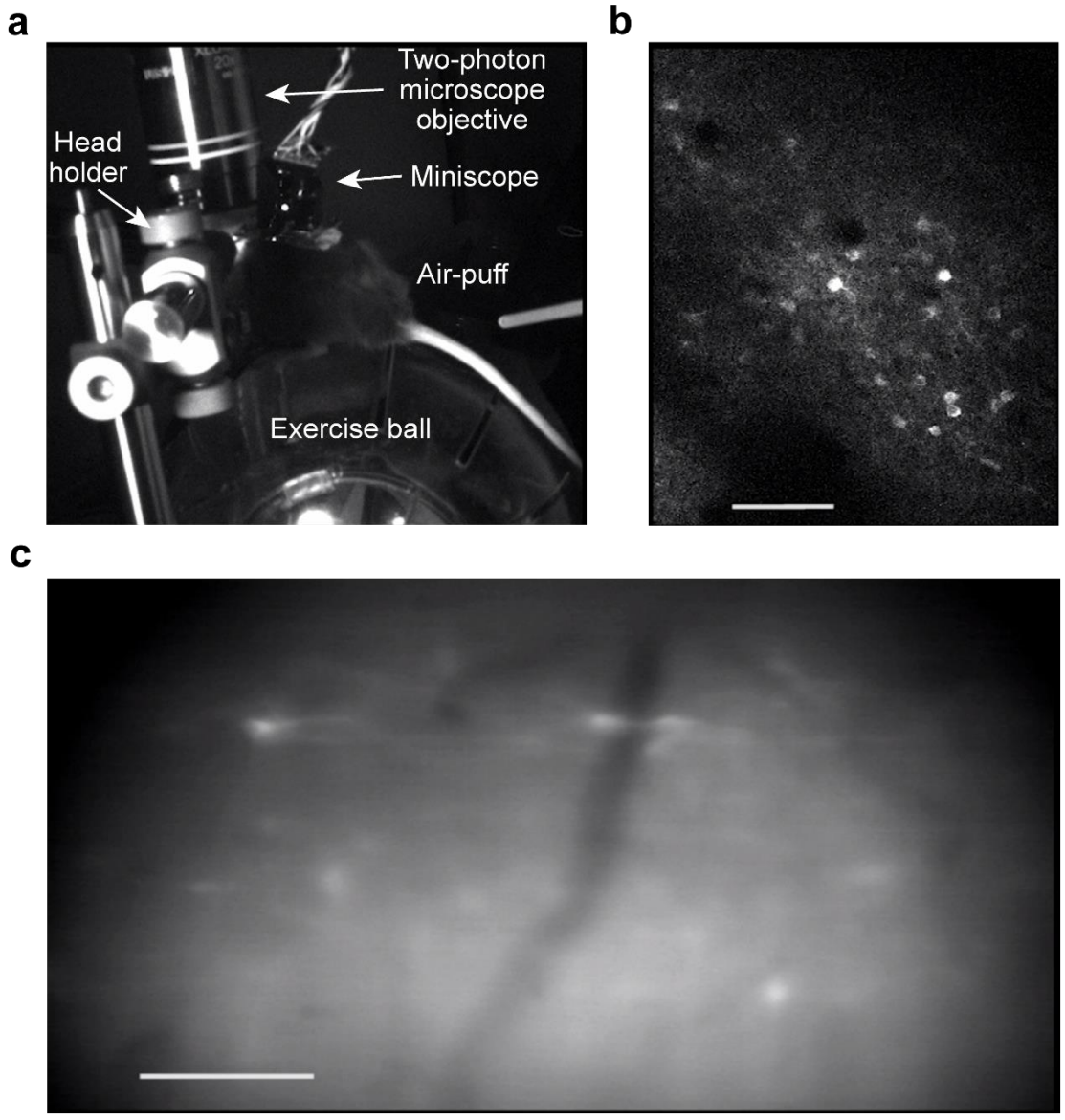

Figure 2.17 Simultaneous optical imaging of cortex and spinal cord. (a) Image of a mouse focally restrained at the level of the head with carrying miniaturized microscopy on the back, and placed on a spherical treadmill under a two-photon microscopy. **(b)** Fluorescence image showing that air-puff-evoked calcium excitation in neuron at layer 2/3 of primary somatosensory cortex. Fluorescence was introduced with AAV1-syn-GCaMP6f. Scale bar, 100 μm. **(c)** Fluorescence image showing that air-puff-evoked calcium excitation in neuron at lamina 1/2 of spinal cord at L4-L5 vertebra level, simultaneously taken with (b). Fluorescence was introduced with AAV9-CaMKII-GCaMP6f. Scale bar, 100 μm.

References

1. Kerr, J.N. & Nimmerjahn, A. Functional imaging in freely moving animals. *Curr. Opin. Neurobiol.* **22**, 45-53 (2012).

2. Dombeck, D.A., Khabbaz, A.N., Collman, F., Adelman, T.L. & Tank, D.W. Imaging large-scale neural activity with cellular resolution in awake, mobile mice. *Neuron* **56**, 43-57 (2007).

3. Flusberg, B.A., Nimmerjahn, A., Cocker, E.D., Mukamel, E.A., Bretto, R.P., Ko, T.H., Burns, L.D., Jung, J.C. & Schnitzer, M.J. High-speed, miniaturized fluorescence microscopy in freely moving mice. *Nat. Methods* **5**, 935-938 (2008).

4. Nimmerjahn, A., Mukamel, E.A. & Schnitzer, M.J. Motor behavior activates Bergmann glial networks. *Neuron* **62**, 400-412 (2009).

5. Ghosh, K.K., Burns L.D., Cocker E.D., Nimmerjahn A., Ziv Y., El Gamal A., & Schnitzer, M.J. Miniaturized integration of a fluorescence microscope. *Nature Methods* **8**, 871-878 (2011).

6. Basbaum, A.I., Bautista, D.M., Scherrer, G. & Julius, D. Cellular and molecular mechanisms of pain. *Cell* **139**, 267-284 (2009).

7. Freeman, M.R. & Rowitch, D.H. Evolving concepts of gliogenesis: a look way back and ahead to the next 25 years. *Neuron* **80**, 613-623 (2013).

8. Todd, A.J. Neuronal circuitry for pain processing in the dorsal horn. *Nat. Rev. Neurosci.* **11**, 823-836 (2010).

9. Braz, J., Solorzano, C., Wang, X. & Basbaum, A.I. Transmitting pain and itch messages: a contemporary view of the spinal cord circuits that generate gate control. *Neuron* **82**, 522-536 (2014).

10. Bardoni, R., Ghirri, A., Zonta, M., Betelli, C., Vitale, G., Ruggieri, V., Sandrini, M & Carmignoto, G. Glutamate-mediated astrocyte-to-neuron signalling in the rat dorsal horn. *J. Physiol.* **588**, 831-846 (2010).

11. Ji, R.R., Berta, T. & Nedergaard, M. Glia and pain: is chronic pain a gliopathy? *Pain* **154**, S10-28 (2013).

12. Molofsky, A.V., Kelly, K.W., Tsai, H.H., Redmond, S.A., Chang, S.M., Madireddy, L., Chan, J.R., Baranzini, S.E., Ullian, E.M. & Rowitch, D.H. Astrocyte-encoded positional cues maintain sensorimotor circuit integrity. *Nature* **509**, 189-194 (2014).

13. Farrar, M.J. Bernstein, I.M., Schlafer D.M., Cleland, T.A., Fetcho, J.R. & Schaffer, C. B. Chronic in vivo imaging in the mouse spinal cord using an implanted chamber. *Nat. Methods* **9**, 297-302 (2012).

14. Kerschensteiner, M., Schwab, M.E., Lichtman, J.W. & Misgeld, T. In vivo imaging of axonal degeneration and regeneration in the injured spinal cord. *Nat. Med.* **11**, 572-577 (2005).

15. Thevenaz, P., Ruttimann, U.E. & Unser, M. A pyramid approach to subpixel registration based on intensity. *IEEE Trans. Image Process.* **7**, 27-41 (1998).

16. Del Barrio, M.G., Bourane, S., Grossmann, K., Schüle, R., Britsch, S., O'Leary, D.D.M. & Goulding, M. A transcription factor code defines nine sensory interneuron subtypes in the mechanosensory area of the spinal cord. *PLoS One* **8**, e77928 (2013).

17. Duan, B. Cheng, L., Bourane, S., Britz, O., Padilla, C., Garcia-Campmany, L., Krashes, M., Knowlton, W., Velasquez, T., Ren, X., Ross, SE., Lowell, B. B., Wang, Y., Goulding, M. & Ma, Q. Identification of spinal circuits transmitting and gating mechanical pain. *Cell* **159**, 1417-1432 (2014).

18. Laffray, S., Pagès, S., Dufour, H., De Koninck, P., De Koninck, Y. & Côtè, D. Adaptive movement compensation for in vivo imaging of fast cellular dynamics within a moving tissue. *PLoS One* **6**, e19928 (2011).

19. Luis-Delgado, O.E., Barrot, M., Rodeau, J.L., Schott, G., Benbouzid, M., Poisbeau, P., Freund-Mercier, M.J. & Lasbennes, F. Calibrated forceps: a sensitive and reliable tool for pain and analgesia studies. *J. Pain* **7**, 32-39 (2006).

20. Mukamel, E.A., Nimmerjahn, A. & Schnitzer, M.J. Automated analysis of cellular signals from large-scale calcium imaging data. *Neuron* **63**, 747-760 (2009).

21. Nimmerjahn, A. & Bergles, D.E. Large-scale recording of astrocyte activity. *Curr. Opin. Neurobiol.* **32**, 95-106 (2015).

22. Ding, F., O'Donnell, J., Thrane, A.S., Zeppenfeld, D., Kang, H., Wang, F & Nedergaard, M. Alpha1-adrenergic receptors mediate coordinated Ca^{2+} signaling of cortical astrocytes in awake, behaving mice. *Cell Calcium* **54**, 387-394 (2013).

23. Paukert, M., Agarwal, A., Cha, J., Doze, V.A., Kang, J.U. & Bergels, D.E. Norepinephrine controls astroglial responsiveness to local circuit activity. *Neuron* **82**, 1263-1270 (2014).

24. Betley, J.N., Xu, S., Cao, Z.F., Gong, R., Magnus, C.J., Yu, Y. & Sternson, S.M. Neurons for hunger and thirst transmit a negative-valence teaching signal. *Nature* **521**, 180-185 (2015).

25. Chen, Y., Lin, Y.C., Kuo, T.W. & Knight, Z.A. Sensory detection of food rapidly modulates arcuate feeding circuits. *Cell* **160**, 829-841 (2015).

26. Jennings, J.H., Ung, R.L., Resendez, S.L., Stamatakis, A.M., Taylor, J.G., Huang, J., Veleta, K., Kantak, P.A., Shilling-Scrivo, K., Ramakrishnan, C., Deisseroth, K., Otte, S. & Stuber, G.D. Visualizing hypothalamic network dynamics for appetitive and consummatory behaviors. *Cell* **160**, 516-527 (2015).

27. Ikeda, H., Stark, J., Fischer, H., Wagner, M., Drdia, R., Jäger, T & Sandkühler, J. Synaptic amplifier of inflammatory pain in the spinal dorsal horn. *Science* **312**, 1659-1662 (2006).

28. Johannssen, H.C. & Helmchen, F. In vivo Ca^{2+} imaging of dorsal horn neuronal populations in mouse spinal cord. *J. Physiol.* **588**, 3397-3402 (2010).

29. Nishida, K., Matsumura, S., Taniguchi, W., Uta, D., Furue, H. & Ito, S. Three-dimensional distribution of sensory stimulation-evoked neuronal activity of spinal dorsal horn neurons analyzed by in vivo calcium imaging. *PLoS One* **9**, e103321 (2014).

30. Niell, C.M. & Stryker, M.P. Modulation of visual responses by behavioral state in mouse visual cortex. *Neuron* **65**, 472-479 (2010).

31. Cirillo, G., De Luca, D. & Papa, M. Calcium imaging of living astrocytes in the mouse spinal cord following sensory stimulation. *Neural Plast.* **2012**, 425818 (2012).

32. Haustein, M.D., Kracun, S., Lu, X.H., Shih, T., Jackson-Weaver, O., Tong, X., Xu, J., Yang X.W., O'Dell, T.J., Ellisman, M.H., Busong, E.A., Looger, L.L. & Khakh, B.S. Conditions and constraints for astrocyte calcium signaling in the hippocampal mossy fiber pathway. *Neuron* **82**, 413-429 (2014).

33. Srinivasan, R., Huang, B.S., Venugopal, S., Johnston, A.D., Chai, H., Zeng, H., Golshani, P. & Khakh, B.S. Ca^{2+} signaling in astrocytes from $Ip3r2^{(-/-)}$ mice in brain slices and during startle responses in vivo. *Nat. Neurosci.* **18**, 708-717

34. Bekar, L.K., He, K. & Nedergaard, M. Locus coeruleus alpha-adrenergic-mediated activation of cortical astrocytes in vivo. *Cereb. Cortex* **18**, 2789-2795 (2008)

35. Hirata, H. & Aston-Jones, G. A novel long-latency response of locus coeruleus neurons to noxious stimuli: mediation by peripheral C-fibers. *J. Neurophysol.* **71**, 1752-1761 (1994)

36. Bourane, S., Duan, S., Koch, S.C., Dalet, A., Garcia-Campmany, L., Kim, E., Cheng, L., Ma, Q. & Goulding, M. Gate control of mechanical itch by a subpopulation of spinal cord interneurons. *Science* **350**, 550-554 (2015).

37. Bourane, S., Grossmann, K.S., Britz, O., Del Barrio, M.G., Stam, F.J., Garcia-Campmany, L., Koch, S. & Goulding, M. Identification of a spinal circuit for light touch and fine motor control. *Cell* **160**, 503-515 (2015).

38. De Pittà, M., Volman, V., Berry, H., Parpura, V., Volterra, A. & Ben-Jacob, E. Computational quest for understanding the role of astrocyte signaling in synaptic transmission and plasticity. *Front. Comput. Neurosci.* **6**, 98 (2012).

39. Dana, H., Mohar, B., Sun, Y., Narayan, S., Gourdus, A., Hasseman, J.P., Ysegaye, G., Holt, G.T., Hu, A., Walpita, D., Patel, R., Machlin, J.J., Bargmann, C.I., Ahrens, M.B., Shreiter, E.R., Jayaraman, V., Looger, L.L., Svobada, K. & Kim D.S. Sensitive red protein calcium indicators for imaging neural activity. *Elife* **5**, e12727 (2016)

40. Shiratori-Hayashi, M., Koga, K., Tozaki-Saitoh, H., Kohro, Y., Toyonaga, H., Yamaguchi, C., Hasegawa, A., Nakahara, T., Hachisuka, J., Akira, S., Okano, H., Furue, M., Inoue, K & Tsuda, M. STAT3-dependent reactive astrogliosis in the spinal dorsal horn underlies chronic itch. *Nat. Med.* **21**, 927-931 (2015).

41. Lu, P., Wang, Y., Graham, L., McHale, K., Gao, M., Wu, D., Brock, J., Blesch, A., Rosenzweig, E.S., Havton, L.A., Zheng, B., Conner, J.M., Marsala, M. & Tuszynski, M.H. Long-distance growth and connectivity of neural stem cells after severe spinal cord injury. *Cell* **150**, 1264-1273 (2012)

42. Bráz, J.M., Wang, X., Guan, Z., Rubenstein, J.L. & Basbaum, A.I. Transplant-mediated enhancement of spinal cord GABAergic inhibition reverses paclitaxel-induced mechanical and heat hypersensitivity. *Pain* **156**, 1084-1091 (2015)

43. Kobat, D., Horton, N.G. & Xu, C. In vivo two-photon microscopy to 1.6-mm depth in mouse cortex. *J. Biomed. Opt.* **16**, 106014 (2011).

44. Andermann, M.L., Gilfoy, N.B., Goldey, G.J., Sachday, R.N., Wölfel, M., McCormick, D.A., Reid, R.C. & Levene, M.J. Chronic cellular imaging of entire cortical columns in awake mice using microprisms. *Neuron* **80**, 900-913 (2013).

45. Horton, N.G., Wang, K., Kobat, D., Clark, C.G., Wise, F.W., Schaffer, C.B. & Xu, C. In vivo three-photon microscopy of subcortical structures within an intact mouse brain. *Nat. Photonics* **7**, doi: 10.1038/nphoton.2012.1336 (2013).

46. Schain, A.J., Hill, R.A. & Grutzendler, J. Label-free in vivo imaging of myelinated axons in health and disease with spectral confocal reflectance microscopy. *Nat. Med.* **20**, 443-449 (2014).

47. Towne, C., Montgomery, K.L., Iyer, S.M., Deisseroth, K. & Delp, S.L. Optogenetic control of targeted peripheral axons in freely moving animals. *PLoS One* **8**, e72691 (2013).

48. Vrontou, S., Wong, A.M., Rau, K.K., Koerber, H.R. & Anderson, D.J. Genetic identification of C fibres that detect massage-like stroking of hairy skin in vivo. *Nature* **493**, 669-673 (2013).

49. Iyer, S.M., Montogomery, K.L., Towne, C., Lee, S.Y., Ramakrishnan, C., Deisseroth, K.& Delp, S.L. Virally mediated optogenetic excitation and inhibition of pain in freely moving nontransgenic mice. *Nat. Biotechnol.* **32**, 274-278 (2014).

50. Nimmerjahn, A. Optical window preparation for two-photon imaging of microglia in mice. *Cold Spring Harb. Protoc.* **2012**, 587-593 (2012).

51. Chum, H.H., Jampachaisri, K., McKeon, G.P., Yeomans, D.C., Pacharinsak, C. & Felt, S.A. Antinociceptive effects of sustained-release buprenorphine in a model of incisional pain in rats (Rattus norvegicus). *J. Am. Assoc. Lab Anim. Sci.* **53**, 193-197 (2014).

52. Knowland, D., Arac, A., Sekiguchi, K.J., Hsu, M., Lutz, S.E., Perrino, J., Steinberg, G.K., barres, B.A., Nimmerjahn, A. & Agalliu, D. Stepwise recruitment of transcellular and paracellular pathways underlies blood-brain barrier breakdown in stroke. *Neuron* **82**, 603-617 (2014).

53. Roberson, D.P., Binshtok, A.M., Blasl, F., Bean, B.P. & Woolf, C.J. Targeting of sodium channel blockers into nociceptors to produce long-duration analgesia: a systematic study and review. *Br. J. Pharmacol.* **164**, 48-58 (2011).

54. Brenneis, C., Kistner, K., Puopolo, M., Segal, D., Roberson, D., Sisignano, M., Labocha, S., Ferreirós N., Strominger, A., Cobos, E.J., Ghasemlou, N., Geisslinger, G., Reeh, P.W., Bean, B.P. & Woolf, C.J. Phenotyping the function of TRPV1-expressing sensory neurons by targeted axonal silencing. *J. Neurosci.* **33**, 315-326 (2013).

Chapter 3
Conclusions

Optical imaging in the spinal cord had previously been restricted to anesthetized animals (1, 2). Anesthesia suppresses cellular activity and precludes animal behavior. My work provides initial demonstration that stable optical measurement of neuronal and astrocyte activity in the spinal cord of behaving mice is feasible using two- and miniaturized one-photon microscopy. It also shows how mechanosensory information is encoded by individual dorsal horn neurons, how different sensory information is represented on the population level, and how astrocytes respond to sensory-evoked neuronal activity. Additionally, it demonstrates that anesthesia disrupts sensory processing in the dorsal horn, and that behavioral changes modulate resting state activity in neurons and astrocytes.

While my work has focused on peripherally evoked activity in a specific subset of dorsal horn neurons, the approach I developed is, in principle, applicable to other spinal cord inputs and cell types. In particular, I expect that the methods I established, combined with new molecular and genetic tools, will enable study of how supraspinal inputs modulate neuronal activity in the dorsal horn or how distinct sensory inputs recruit different genetically defined sets of neurons or neural circuits. Because I showed that repeated optical imaging over days to weeks is feasible, study of how changes in dorsal horn activity relate to aberrant sensation in disease, or to recovery from injury-related sensory impairments, seems possible using established mouse models of disease or spinal cord injury.

Likewise, while my work has focused on dorsal horn astrocytes the methods I developed are applicable to other regions, such as white matter, or other types of glial cells, such as microglia. Although dorsal horn microglia do not seem to show clear sensory-evoked Ca^{2+} transients in healthy animals (unpublished observations), they may do so under pathological conditions in which these cells become reactive (3). My approaches should, in principle, also

enable study of how satellite glial cells in the DRG respond to sensory stimulation. Like astrocytes, satellite glial cells structurally and chemically interact with primary afferent neurons and play crucial roles in sensory processing under healthy and pathological conditions (4).

While the availability of new red-shifted calcium indicators is already allowing study of how neuronal and astrocyte activity patterns relate to each other (unpublished observations), the availability of new synthetic or genetically encoded neurotransmitter indicators (e.g., for opioid or ATP signaling) will soon allow direct visualization of how different signaling events/behaviors trigger distinct forms of neuronal or astrocyte excitation in various cellular compartments. Similarly, they will allow study of how release of soluble messengers from astrocytes influences sensory or pain processing in the spinal cord (5).

In summary, my work provides an avenue for systematic study of how diverse cell types in the spinal dorsal horn process sensory information under natural conditions. By producing a dynamic picture of the functioning spinal cord the imaging approaches I developed and their future extensions (e.g., combined monitoring and manipulation of cellular activity in freely moving animals, or concomitant optical measurement of cellular activity in anatomically connected brain and spinal cord networks) promise to further our understanding of the computations underlying normal sensory processing, and the pathologic changes provoked by disorders that affect sensation.

References

1. Johannssen, H.C. & Helmchen, F. In vivo Ca^{2+} imaging of dorsal horn neuronal populations in mouse spinal cord. *J. Physiol.* **588**, 3397-3402 (2010).

2. Nishida, K., Matsumura, S., Taniguchi, W., Uta, D., Furue, H. & Ito, S. Three-dimensional distribution of sensory stimulation-evoked neuronal activity of spinal dorsal horn neurons analyzed by in vivo calcium imaging. *PLoS One* **9**, e103321 (2014).

3. Guan, Z., Kuhn, J.A., Wang, X., Colquitt, B., Solorzano, C., Vaman, S., Guan, A.K., Evans-Reinsch, Z., Braz, J., Devor, M., Abboud-Werner, S.L., Lanier, L.L., Lomvardas, S. & Basbaum, A.I. Injured sensory neuron-derived CSF1 induces microglial proliferation and DAP12-dependent pain. *Nat. Neurosci.* **19**, 94-101 (2016).

4. Ohara, P. T., Vit, J-P., Bhargava, A., Romero, M., Sundberg, C., Charles, A. C., & Jasmin, L. (2009). Gliopathic Pain: When Satellite Glial Cells Go Bad. *Neuroscientist* **15**, 450–463 (2009).

5. Kronschläger, M.T., Drdla-Schutting, R., Gassner, M., Honsek, S.D., Teuchmann, H.L. & Sandkühler, J. Gliogenic LTP spreads widely in nociceptive pathways. *Science* **354**, 1144-1148 (2016).